

# Significant Gas-to-Dust Ratio Asymmetry and Variation in the Disk of HD 142527 and the Indication of Gas Depletion

Takayuki MUTO,<sup>1</sup> Takashi TSUKAGOSHI,<sup>2</sup> Munetake MOMOSE,<sup>2</sup> Tomoyuki HANAWA,<sup>3</sup> Hideko NOMURA,<sup>4</sup> Misato FUKAGAWA,<sup>5</sup> Kazuya SAIGO,<sup>6</sup> Akimasa KATAOKA,<sup>5,7</sup> Yoshimi KITAMURA,<sup>8</sup> Sanemichi Z. TAKAHASHI,<sup>9</sup> Shu-ichiro INUTSUKA,<sup>10</sup> Taku TAKEUCHI,<sup>4</sup> Hiroshi KOBAYASHI<sup>10</sup> Eiji AKIYAMA,<sup>5</sup> Mitsuhiro HONDA,<sup>11</sup> Hideaki FUJIWARA,<sup>12</sup> and Hiroshi SHIBAI<sup>13</sup>

<sup>1</sup>Division of Liberal Arts, Kogakuin University, 1-24-2 Nishi-Shinjuku, Shinjuku-ku, Tokyo 163-8677

<sup>2</sup>College of Science, Ibaraki University, 2-1-1 Bunkyo, Mito, Ibaraki 310-8512

<sup>3</sup>Center for Frontier Science, Chiba University, 1-33 Yayoi-cho, Inage-ku, Chiba 263-8522

<sup>4</sup>Department of Earth and Planetary Sciences, Tokyo Institute of Technology, Meguro-ku, Tokyo 152-8551

<sup>5</sup>National Astronomical Observatory of Japan, 2-21-1 Osawa, Miaka, Tokyo 181-8588

<sup>6</sup>Department of Physical Science, Graduate School of Science, Osaka Prefecture University, 1-1 Gakuen-cho, Naka-ku, Sakai, Osaka 599-8531, Japan

<sup>7</sup>Institute for Theoretical Astrophysics, Heidelberg University, Albert-Ueberle-Strasse 2, 69120, Heidelberg, Germany

<sup>8</sup>Institute of Space and Astronautical Science, Japan Aerospace Exploration Agency, 3-1-1 Yoshinodai, Chuo-ku, Sagami-hara, Kanagawa 252-5210

<sup>9</sup>Astronomical Institute, Tohoku University, 6-3, Aramaki, Aoba-ku, Sendai, Miyagi 980-8587

<sup>10</sup>Department of Physics, Graduate School of Science, Nagoya University, Furo-cho, Chikusa-ku, Nagoya 464-8601

<sup>11</sup>Department of Mathematics and Physics, Kanagawa University, 2946 Tsuchiya, Hiratsuka, Kanagawa 259-1293

<sup>12</sup>Subaru Telescope, 650 North Aohoku Place, Hilo, HI 96720, USA

<sup>13</sup>Graduate School of Science, Osaka University, 1-1 Machikaneyama, Toyonaka, Osaka 560-0043

\*E-mail: muto@cc.kogakuin.ac.jp

Received ; Accepted

## Abstract

We investigate the dust and gas distribution in the disk around HD 142527 based on ALMA observations of dust continuum,  $^{13}\text{CO } J = 3 - 2$ , and  $\text{C}^{18}\text{O } J = 3 - 2$  emission. The disk shows strong azimuthal asymmetry in the dust continuum emission, while gas emission is more symmetric. In this paper, we investigate how gas and dust are distributed in the dust-bright northern part of the disk and in the dust-faint southern part. We construct two axisymmetric disk models. One reproduces the radial profiles of the continuum and the velocity moments 0 and 1 of CO lines in the north and the other reproduces those in the south. We have found that the dust is concentrated in a narrow ring having  $\sim 50$  AU width (in FWHM;  $w_d = 30$  AU in

our parameter definition) located at  $\sim 170 - 200$  AU from the central star. The dust particles are strongly concentrated in the north. We have found that the dust surface density contrast between the north and south amounts to  $\sim 70$ . Compared to the dust, the gas distribution is more extended in the radial direction. We find that the gas component extends at least from  $\sim 100$  AU to  $\sim 250$  AU from the central star, and there should also be tenuous gas remaining inside and outside of these radii. The azimuthal asymmetry of gas distribution is much smaller than dust. The gas surface density differs only by a factor of  $\sim 3 - 10$  between the north and south. Hence, gas-to-dust ratio strongly depends on the location of the disk:  $\sim 30$  at the location of the peak of dust distribution in the south and  $\sim 3$  at the location of the peak of dust distribution in the north. Despite large uncertainties, the overall gas-to-dust ratio is inferred to be  $\sim 10 - 30$ , indicating that the gas depletion may have already been under way.

**Key words:** stars: individual (HD 142527) — stars: pre-main-sequence — planetary systems: protoplanetary disks — submillimeter: planetary systems — radiative transfer

## 1 Introduction

Transitional disks are circumstellar disks having an inner hole of dust emission, and are considered to be in the evolutionally phase from gas-rich protoplanetary disks to gas-poor debris ones (Strom et al. 1999; Calvet et al. 1999; Andrews et al. 2011). This class of disks have attracted much attention as valuable samples to study the disk evolution and planet formation processes. Among a number of transitional disk objects, HD 142527 is a subject of intense study. It is a Herbig Fe star (Waelkins et al. 1996) harboring a disk with a wide dust cavity with the radius of  $\gtrsim 100$  AU (Fukagawa et al. 2006; Fujiwara et al. 2006; Verhoeff et al. 2011; Rameau et al. 2012; Casassus et al. 2012). The stellar mass is  $\sim 2.2 M_{\odot}$  and the age is 5 Myr if we adopt  $d = 140$  pc considering the association to Sco OB2 (Fukagawa et al. 2006; Verhoeff et al. 2011; Mendigutía et al. 2014). Recent observations have revealed the possible existence of low-mass companion ( $\sim 0.1 - 0.4 M_{\odot}$ ) at 13 AU from the central star (Biller et al. 2012; Rodigas et al. 2014).

The disk around HD 142527 shows several interesting features. The near infrared scattered light image of the disk shows extended emission out to  $\gtrsim 300$  AU and large-scale spiral features are observed (Fukagawa et al. 2006; Casassus et al. 2012; Canovas et al. 2013; Rodigas et al. 2014), hinting that some dynamical activity is taken place in the disk (Casassus et al. 2012). ALMA observations of dust continuum emission show significant azimuthal asymmetry with a bright horseshoe-like emission in the northern part of the disk (Casassus et al. 2013; Fukagawa et al. 2013; Perez et al. 2015). It is indicated that large grains are concentrated in this northern region (Casassus et al. 2015). In the vicinity of the central star, a stream-like features in  $\text{HCO}^+ J = 4 - 3$  emission (Casassus et al. 2013) and a point source of dust emission (Fukagawa et al. 2013) are observed.  $\text{HCN } J = 4 - 3$  and  $\text{CS } J = 7 - 6$  emissions are also spatially resolved with ALMA (van der Plas et al. 2014).

Fukagawa et al. (2013) presented the results of ALMA band 7 observations of dust continuum and gas emission in  $^{13}\text{CO } J = 3 - 2$  and  $\text{C}^{18}\text{O } J = 3 - 2$ . On the basis of the very bright dust continuum emission ( $\gtrsim 20$  K) in the northern part, they discussed two possibilities for the disk gas distribution. One is that the gas-to-dust mass ratio is less than 100 at least in the northern part and significant dust concentration occurs. The other is that the gas-to-dust mass ratio is standard value of 100 so the disk gas mass can be high enough for the onset of gravitational instability. In either case, the disk is likely to be in the process of ongoing planet formation.

It is important to pin down the amount of gas and dust by means of detailed modeling. In this paper, we derive the gas and dust distribution based on ALMA Cycle 0 Band 7 observations of HD 142527 using more detailed modeling of gas and dust emission than Fukagawa et al. (2013). We derive the dust distribution from the continuum emission and the gas distribution from the CO emission in order to obtain the gas-to-dust ratio in the northern and the southern part of the disk.

The paper is constructed as follows. In section 2, we summarize the results of observations. In section 3, we describe the method of modeling. In sections 4 and 5, we present the modeling results of dust and gas distribution, respectively. In section 6, we discuss implications of our best-fit model. Section 7 is for summary.

**Table 1.** Gaussian parameters (equation (1)) that fit the radial profiles of dust continuum emission in the brightest and the faintest directions. The parameters  $r_0$  and  $w$  are given in the unit of AU assuming that the distance to HD 142527 is 140 pc.

$PA$	$I_p$ [Jy/asec <sup>2</sup> ]	$r_{0,obs}$ [AU]	$w_{obs}$ [AU]
11 – 31° (North profile)	1.2	152	51
211 – 231° (South profile)	0.050	174	51

## 2 Observation

### 2.1 Observation and Data Reduction

ALMA Band 7 Cycle 0 observations of HD 142527 (RA=J2000 15h56m41.9, DEC=J2000 -42d19m23.3) were carried out in the extended array configuration with a maximum baseline of about 480 m. The observations consisted of six scheduling blocks during the period from June to August 2012. The correlator was configured to store dual polarizations in four separate spectral windows with 469 MHz of bandwidth and 3840 channels each, and their central frequencies are 330.588, 329.331, 342.883 and 342.400 GHz, respectively, to target the molecular lines of  $^{13}\text{CO } J = 3 - 2$  and  $\text{C}^{18}\text{O } J = 3 - 2$ . The resultant channel spacing for the lines was 122 kHz, corresponding to  $0.12 \text{ km s}^{-1}$  in velocity at these frequencies, but the effective spectral resolution was lower by a factor of around 2 ( $\sim 0.2 \text{ km s}^{-1}$ ) because of Hanning smoothing. The continuum data from all the spectral windows were aggregated and treated as a single data set of 336 GHz in central frequency and 1.8 GHz in bandwidth. The on-source integration after flagging aberrant data was 3.0 h.

Calibration and reduction of the data were made with the Common Astronomy Software Applications (CASA) version 3.4, in almost the same way as that in Fukagawa et al. (2013). Self-calibration was performed for the continuum to improve the sensitivity and image fidelity, and the final gain solution was also applied to  $^{13}\text{CO}$  and  $\text{C}^{18}\text{O}$  data. The only difference from Fukagawa et al. (2013) was the visibility weighting applied in the final step of the imaging; we adopted in this study the Briggs weighting with a robust parameter of 0.5 to best recover the weak and extended components of the emission. The size in FWHM and the position angle for the major axis of each synthesized beam were  $0''.47 \times 0''.40 = 60 \text{ AU} \times 56 \text{ AU}$  ( $PA = 59.9^\circ$ ),  $0''.50 \times 0''.42 = 70 \text{ AU} \times 59 \text{ AU}$  ( $PA = 57.4^\circ$ ) and  $0''.50 \times 0''.42 = 70 \text{ AU} \times 59 \text{ AU}$  ( $PA = 60.6^\circ$ ), for the continuum at 336 GHz,  $^{13}\text{CO}$  and  $\text{C}^{18}\text{O}$ , respectively. Further details on bandpass and gain calibrations are described in Fukagawa et al. (2013). The rms noise is  $0.13 \text{ mJy beam}^{-1}$  for the continuum whereas it is 6.1 and  $8.3 \text{ mJy beam}^{-1}$  in the  $0.12 \text{ km s}^{-1}$  wide channels for the line emission of  $^{13}\text{CO}$  and  $\text{C}^{18}\text{O}$ , respectively.

### 2.2 Results of Dust Continuum Emission

Figure 1 shows the continuum map, which looks quite similar to that presented by Fukagawa et al. (2013). The outer asymmetric ring as well as an inner unresolved component are detected, and these are separated by a radial gap. The position of the unresolved component coincides with the velocity centroid of  $^{13}\text{CO } J = 3 - 2$  (section 2.3), and it is regarded as the stellar position in the following. The radial profiles of surface brightness is well described by a Gaussian function, and the brightest and faintest of their peaks are located at  $PA \approx 23^\circ$  and  $PA \approx 223^\circ$ , respectively (see also figure 4 of Fukagawa et al. (2013)). The averaged surface brightness profiles  $I(r)$  in  $PA = 11^\circ - 31^\circ$  and  $211^\circ - 231^\circ$  are fitted by

$$I(r) = I_p \exp \left[ -\frac{(r - r_{0,obs})^2}{w_{obs}^2} \right], \quad (1)$$

where  $r$  is the angular distance from the star,  $r_{0,obs}$  is the peak position and  $w_{obs}$  is the width of the Gaussian. The best-fit profiles are shown in figure 2 and the best-fit parameters are summarized in table 1. As shown in table 1, the contrast in  $I_p$  is 24 between these two position angles. In the following, we refer to the averaged profiles in the section of  $11^\circ < PA < 31^\circ$  as “north profile” and that in  $211^\circ < PA < 231^\circ$  as “south profile” (see the right panel of figure 1).

### 2.3 Results of $^{13}\text{CO}$ and $\text{C}^{18}\text{O } J = 3 - 2$ Emission

Figures 3 and 4 show the moment maps of the  $^{13}\text{CO } J = 3 - 2$  and  $\text{C}^{18}\text{O } J = 3 - 2$  emission, respectively. Moments 0, 1, and 2 correspond to the integrated intensity, intensity-weighted mean velocity, and velocity dispersion, respectively. As shown in the appendix, the emission above  $5\sigma$  level is detected in  $v_{LSR} = (0.64 - 7.00) \text{ km s}^{-1}$  in  $^{13}\text{CO}$  and  $v_{LSR} = (1.24 - 6.16) \text{ km s}^{-1}$  in  $\text{C}^{18}\text{O}$ . The azimuthal asymmetry is weak in the moment 0 map although the northern part tends to be slightly weaker, possibly due

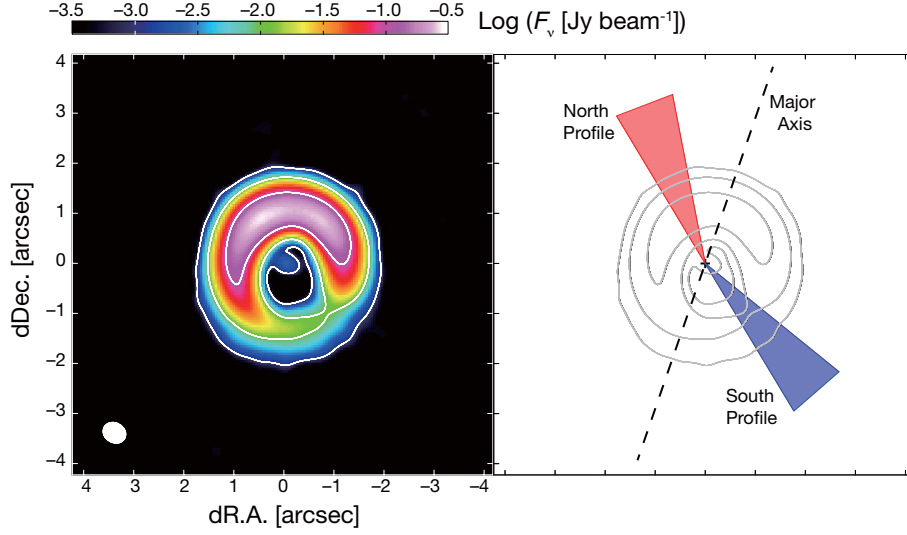


**Fig. 1.** (Left) Map of the continuum emission at 336 GHz with the Briggs weighting with the robust parameter of 0.5. The synthesized beam,  $0''.47 \times 0''.40$  with the major axis  $PA = 59.9^\circ$ , is indicated by the white ellipse in the bottom left corner. The contours correspond to 1, 10 and 100  $\text{mJy beam}^{-1}$ . The  $1\sigma$  level is  $0.13 \text{ mJy beam}^{-1}$ . (Right) The position angle of the major axis is indicated by dashed line. The regions where the azimuthal average is taken to obtain the north profiles ( $PA = 11^\circ - 31^\circ$ ) and the south profiles ( $PA = 211^\circ - 231^\circ$ ) are indicated by red and blue hatches, respectively. Contours are the same with the left panel.

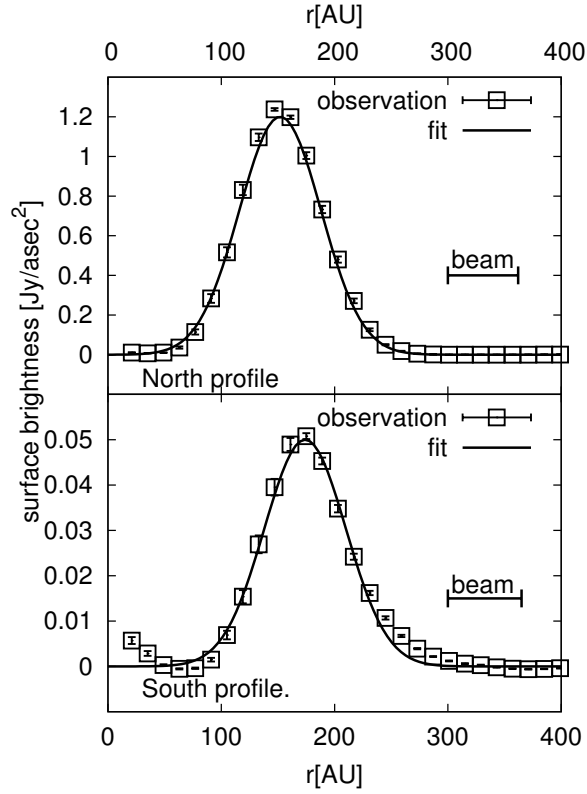


**Fig. 2.** Radial profiles of surface brightness of the continuum emission at 336 GHz in  $PA = 11 - 31^\circ$  (top panel, squares) and  $PA = 211 - 231^\circ$  (bottom panel, squares). Solid lines indicate the best-fit Gaussian function (see Table 1 for parameters). Error bars indicate the standard deviation after the averaging over 20 degrees in  $PA$ .

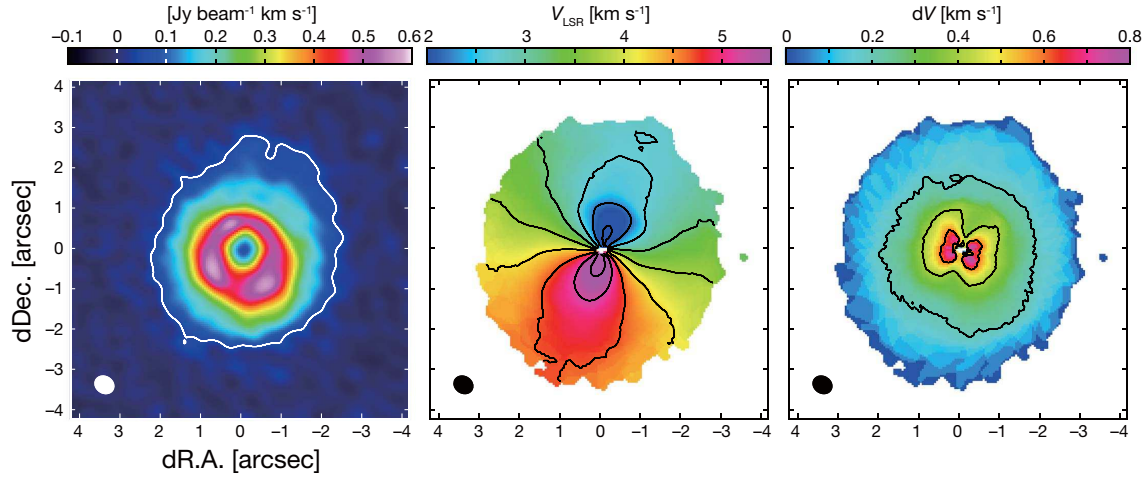


**Fig. 3.** Moment maps of the  $^{13}\text{CO } J = 3 - 2$  line. (left) Moment 0 map, integrated over the velocity range of  $v_{\text{LSR}} = (0.40 - 7.00) \text{ km s}^{-1}$ . The white contour shows the  $5\sigma$  level ( $48 \text{ mJy beam}^{-1} \text{ km s}^{-1}$ ). (middle) Moment 1 map, created by the emission above the  $5\sigma$  level in channel maps of  $0.12 \text{ km s}^{-1}$  resolution (figure 32-34 in appendix). The contours along  $PA \approx 71^\circ$  are those of the systemic velocity ( $v_{\text{LSR}} = 3.7 \text{ km s}^{-1}$ ), and the contour spacing is  $0.5 \text{ km s}^{-1}$ . (right) Moment 2 map, created by the emission above the  $5\sigma$  level in channel maps of  $0.12 \text{ km s}^{-1}$  resolution. Contour starts at  $0.2 \text{ km s}^{-1}$ , and its spacing is  $0.2 \text{ km s}^{-1}$ . The synthesized beam,  $0''.50 \times 0''.42$  with the major axis  $PA = 57.4^\circ$ , is indicated by the ellipse in the bottom left corner of each panel.

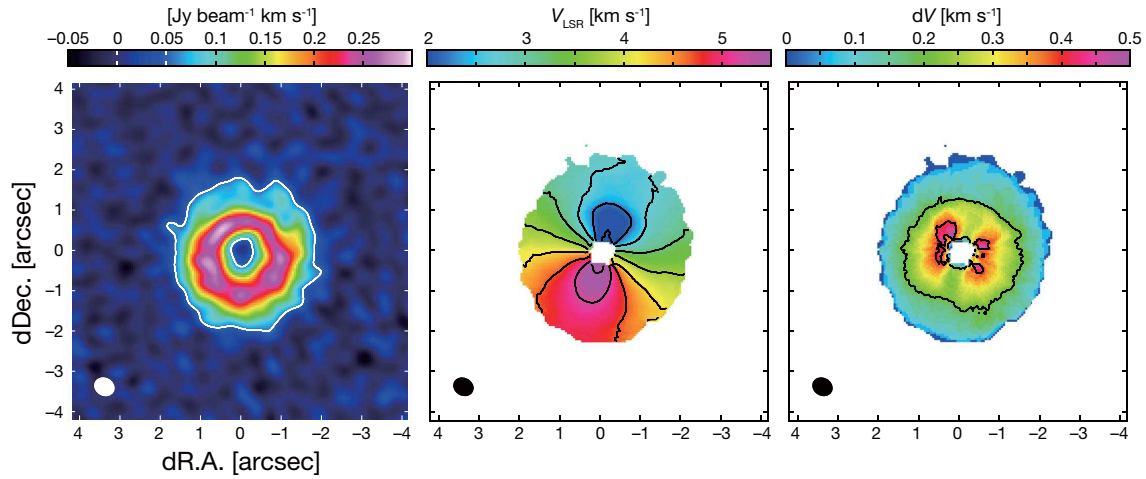


**Fig. 4.** Moment maps of the  $\text{C}^{18}\text{O } J = 3 - 2$  line. (left) Moment 0 map, integrated over the velocity range of  $v_{\text{LSR}} = (1.0 - 6.40) \text{ km s}^{-1}$ . The white contour shows the  $5\sigma$  level ( $55 \text{ mJy beam}^{-1} \text{ km s}^{-1}$ ). (middle) Moment 1 map, created by the emission above the  $5\sigma$  level in channel maps of  $0.12 \text{ km s}^{-1}$  resolution (figure 35-36 in appendix). The contours along  $PA \approx 71^\circ$  are those of the systemic velocity ( $v_{\text{LSR}} = 3.7 \text{ km s}^{-1}$ ), and the contour spacing is  $0.5 \text{ km s}^{-1}$ . (right) Moment 2 map, created by the emission above the  $5\sigma$  level in channel maps of  $0.12 \text{ km s}^{-1}$  resolution. Contours at  $0.2$  and  $0.4 \text{ km s}^{-1}$  are shown. The synthesized beam,  $0''.50 \times 0''.42$  with the major axis  $PA = 60.6^\circ$ , is indicated by the ellipse in the bottom left corner of each panel.

to higher continuum levels. Furthermore, the line emission ( $^{13}\text{CO}$ , in particular) is clearly detected in the inner regions down to  $r \approx 20 \text{ AU}$  ( $0''.15$ ) as well as the outer regions out to  $r \approx 400 \text{ AU}$  ( $2''.8$ ). The velocity distribution revealed in moments 1 and 2 is consistent with a disk in Keplerian rotation. A constant (systemic) velocity of  $3.7 \text{ km s}^{-1}$  is found along  $PA = 71^\circ \pm 2^\circ$  in the moment 1 maps, and this is regarded as the direction of the minor axis of the system. The position-velocity (P-V) diagram along the major axis ( $PA = -19^\circ$ ) is explained well by Keplerian rotation with stellar mass of  $2.2 M_\odot$  and the inclination angle of  $27^\circ$ , as described in detail in the appendix (see also Fukagawa et al. 2013; Perez et al. 2015). We adopt these values for  $PA$  of the major axis and inclination of the system throughout this paper.

Figure 5 shows the north and south profiles of the moments 0 and 1, which will be the main focus of the modeling described in later sections. It is clear that the moment 0 profiles of both  $^{13}\text{CO}$  and  $\text{C}^{18}\text{O}$  are very different from those of dust continuum emission; these are more extended than the Gaussian-like dust emission profiles. The moment 1 profiles of these two lines agree with each other in  $100 \text{ AU} \leq r \leq 280 \text{ AU}$ , indicating that both these lines successfully reveal the Keplerian rotation in the regions where the

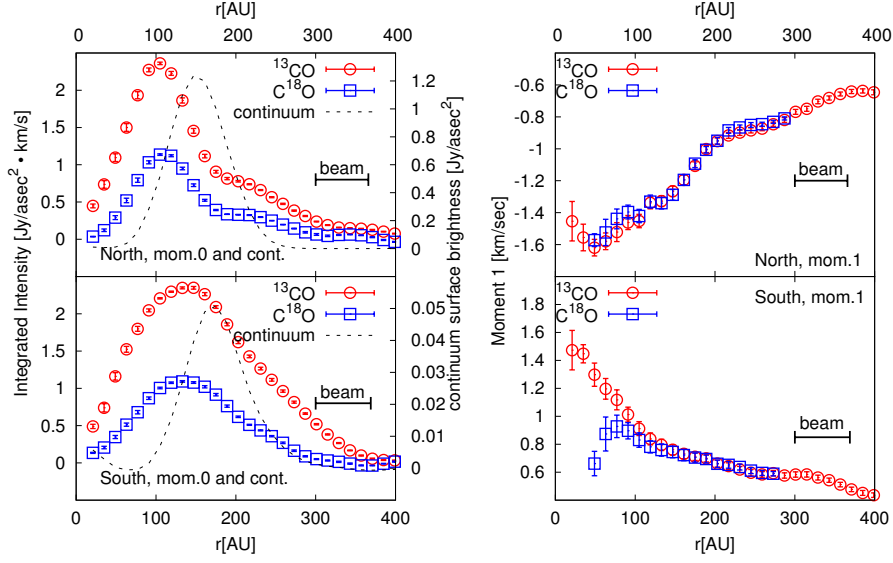


**Fig. 5.** The north (top row) and the south (bottom row) radial profiles of the observed moment 0 (left panels) and moment 1 (right panels) of  $^{13}\text{CO}$  (red circles) and  $\text{C}^{18}\text{O}$  (blue squares). The systemic velocity of 3.7 km/s is subtracted in calculating the moment 1 profiles. Error bars indicate the standard deviation after the averaging over 20 degrees in  $PA$ . The radial profiles of the continuum emission is overplotted in the moment 0 radial profiles for comparison.

emission is detected with a high signal-to-noise ratio (S/N). The moment 1 profile of  $^{13}\text{CO}$  further reveals the gas motion down to  $r \approx 20$  AU and out to  $r \approx 400$  AU. As discussed in the subsequent sections, this indicates the existence of tenuous gas components in these inner and outer regions. The  $^{13}\text{CO}$  line has larger moments 0 and 2 in almost all the positions than the  $\text{C}^{18}\text{O}$ . This is because  $^{13}\text{CO}$  has a larger optical depth at every velocity channel and hence has a broader line profile than  $\text{C}^{18}\text{O}$  (see also section 6.2.2)

### 3 Method of Modeling

Our goal is to find density and temperature distribution of the disk around HD 142527 based on the continuum and CO line emission profiles described in the previous section. We construct axisymmetric models that can reproduce similar radial brightness profiles in the direction where dust emission is the brightest (north profile) and the faintest (south profile) since the model that fully accounts for the azimuthal asymmetry can be very complex. This approach is similar to that taken by Bruderer et al. (2013) in making the model for the disk around Oph IRS 48, which also exhibits strong azimuthal asymmetry.

#### 3.1 Dust Distribution Models

We first derive dust density and temperature distributions from the continuum emission under the assumption that the disk is in thermal and hydrostatic equilibrium. For simplicity, the gas-to-dust ratio is assumed to be uniform in the vertical direction and the gas temperature is assumed to be the same as dust. In other words, we have ignored dust sedimentation (e.g., Dubrulle et al. 1995) and temperature difference between gas and dust in the low density upper layers (e.g., Kamp and Dullemond 2004; Nomura and Miller 2005). We note that the gas-to-dust ratio can vary in the radial direction, which is the main focus of the modeling of gas observations (see sections 3.2 and 5). The disk is assumed to be heated only by stellar irradiation, since viscous heating is less important in the region considered in this paper. The star is assumed to have the effective temperature of  $T_{\text{eff}} = 6250$  K and the radius of  $R = 3.8 R_{\odot}$  (Verhoeff et al. 2011).<sup>1</sup> We solved the zeroth and first order moment equations of the radiative transfer (M1 method, see Kanno et al. 2013). We use 226 colors in the wavelength range of  $0.1 \mu\text{m} \leq \lambda \leq 3.16$  mm, resulting in the spectral resolution of  $\Delta \log \lambda = 0.02$  (i.e.,  $\lambda/\Delta\lambda = 21.7$ ). The computational box covers  $30 \text{ AU} \leq r \leq 410 \text{ AU}$  and  $|z| \leq 120 \text{ AU}$  with the spatial resolution of 2 AU in the cylindrical coordinates. The disk is assumed to be symmetric with respect to the midplane.

The dust is assumed to consist of silicate, carbonaceous grains, and water ice having the mass fractional abundance of  $\zeta_{\text{sil}} = 0.0043$ ,  $\zeta_{\text{carbon}} = 0.0030$ , and  $\zeta_{\text{ice}} = 0.0094$ , respectively, which are consistent with solar elemental abundance (Anders and Grevesse

<sup>1</sup> The stellar parameters are updated in Mendigutía et al. (2014), but the stellar luminosity is within the error for the parameters described here.



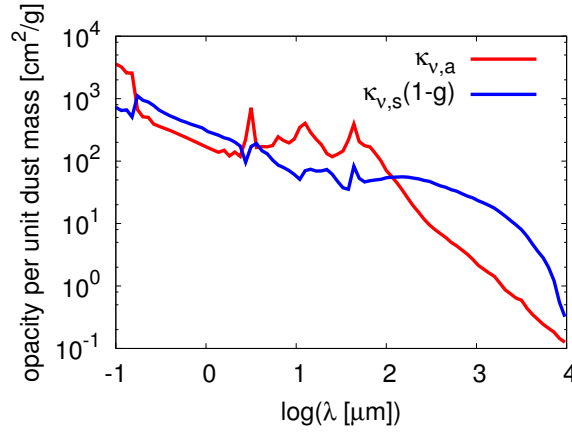


Fig. 6. The absorption (red) and the effective scattering (blue; see text for definition) coefficients for the dust model used in this paper.

1989). The dust particles are assumed to have the power-law size distribution of  $\propto a^{-3.5}$  with the maximum size of  $a_{\max} = 1$  mm (Nomura and Miller 2005). Figure 6 shows the absorption ( $\kappa_{\nu,a}$ ) and the effective scattering coefficients in units of  $\text{cm}^2$  per unit gram of dust. Here, we define the effective scattering coefficient as  $\kappa_{\nu,s}(1-g)$ , where  $\kappa_{\nu,s}$  is the scattering coefficient and  $g = \langle \cos \theta \rangle$  is the scattering asymmetry factor.<sup>2</sup> The model with the maximum dust size of 1 mm gives the large value of opacity at sub-mm range (Aikawa and Nomura 2006). Consequently, the dust mass evaluated in this paper should be close to the lowest. Our opacity at  $870 \mu\text{m}$  has values of  $\kappa_a = 2.9 \text{ cm}^2/\text{g}$  with  $\beta \sim 1.2$  at  $0.3 \text{ mm} \leq \lambda \leq 1 \text{ cm}$  and  $\kappa_s(1-g) = 26 \text{ cm}^2/\text{g}$  per unit dust mass. The absorption coefficient at  $870 \mu\text{m}$  is 20% smaller than the value adopted by Beckwith et al. (1990), which is  $\sim 3.5 \text{ cm}^2/\text{g}$  per unit dust mass. We also note that the effective scattering coefficient is large compared to the absorption one in the sub-mm range since the maximum dust size is comparable with the wavelength.

The dust surface density is assumed to have the form

$$\Sigma_d(r) = \Sigma_{d,0} \exp \left[ - \left( \frac{r - r_d}{w_d} \right)^2 \right] \quad (2)$$

since the radial profile of the continuum emission is well approximated by a Gaussian function. For an assumed set of parameters  $(\Sigma_{d,0}, r_d, w_d)$ , we obtain the spatial distribution of dust density  $\rho_d(r, z)$ , temperature  $T(r, z)$ , and the radiation energy density  $J_\nu(r, z)$  for the 226 colors at each grid cell.

The expected observed surface brightness profiles of dust continuum emission is obtained by ray-tracing. The surface brightness  $I_\nu$  at frequency  $\nu$  is calculated by solving

$$\frac{dI_\nu}{ds} = -\rho_d \chi_\nu [I_\nu - S_\nu], \quad (3)$$

where  $s$  is the coordinate along the line of sight,  $\chi_\nu$  is the extinction by absorption and (effective) scattering,  $\chi_\nu = \kappa_{\nu,a} + (1-g)\kappa_{\nu,s}$ . The source function,  $S_\nu$ , is given by

$$S_\nu = (1 - \omega_\nu) B_\nu(T) + \omega_\nu J_\nu, \quad (4)$$

where  $\omega_\nu = (1-g)\kappa_{\nu,s}/\chi_\nu$  is the (effective) albedo<sup>3</sup> and  $B_\nu(T)$  is the Planck function. The second term in equation (4) represents the scattered light, and the scattering is assumed to be isotropic for simplicity. The optical depth  $\tau_\nu$  along the line of sight is given by

$$\frac{d\tau_\nu}{ds} = -\chi_\nu \rho_d. \quad (5)$$

We compute the model image by using  $(N_R, N_\Phi) = (128, 128)$  rays covering  $35 \text{ AU} < R < 400 \text{ AU}$  and  $0 < \Phi < 2\pi$  region, where  $(R, \Phi)$  are the polar coordinates on the sky-plane with the central star at the origin. We use the inclination angle of  $27^\circ$ , as described in section 2

<sup>2</sup> We have left the term  $(1-g)$  for consistency with the M1 method. See Mihalas and Mihalas (1984); González, Audit and Huynh (2007) for the appearance of  $(1-g)$  factor in the M1 method.

<sup>3</sup> With the dust model of  $a_{\max} = 1$  mm, the value of  $\bar{\omega}_\nu = \kappa_s/(\kappa_a + \kappa_s)$  and  $\omega_\nu$  given in the main text differs only by  $\sim 5\%$  at the wavelengths of interest.

For comparison with observations, we convolve the model images with the Gaussian function of the same beam size and orientation with the observations. We extract the radial surface brightness profiles from the convolved image and compare them with observations. We iterate this procedure until the given set of parameters ( $\Sigma_{d,0}, r_d, w_d$ ) reproduces the observed profiles shown in figure 2 reasonably well.

### 3.2 Gas Distribution Models

We then derive the gas distribution that accounts for both moments 0 (integrated intensity) and 1 (intensity-weighted mean velocity) radial profiles in the north and south directions. We have chosen these moments of the line emission because they are least affected by beam dilution. It should also be noted that the observed moment 2 profiles contains the uncertainty coming from the choice of cutoff levels when producing the moment map from the data.

In later sections, we show that uniform gas-to-dust ratio models do not reproduce the observations. Therefore, we assume that the gas density  $\rho_g(r, z)$  is given by

$$\rho_g(r, z) = \xi(r)\rho_d(r, z), \quad (6)$$

where  $\xi(r)$  represents the gas-to-dust ratio at each radius. The gas surface density  $\Sigma_g(r)$  is then given by

$$\Sigma_g(r) = \xi(r)\Sigma_d(r) \quad (7)$$

In later sections, we look for the forms of  $\xi(r)$ , or, equivalently, the form of  $\Sigma_g(r)$ , that best reproduces the observed radial profiles of moments 0 and 1.

We assume that the gas rotation is Keplerian at the disk midplane,

$$v_{\text{rot}}(r) = 3.13 \left( \frac{r}{200 \text{ AU}} \right)^{-1/2} [\text{km s}^{-1}], \quad (8)$$

where  $3.13 \text{ km s}^{-1}$  is the Kepler velocity at 200 AU around a  $2.2 M_\odot$  star. Rotation velocity can be slightly different from Keplerian due to, for example, radial pressure gradient force, but the difference is at most of the order of thermal velocity ( $\sim 10\%$  of the Kepler rotation velocity), which is hardly observed with current velocity resolution. Gas temperature  $T(r, z)$  is assumed to be the same as the dust temperature as mentioned in section 3.1.

The expected brightness of line emission is calculated with ray-tracing methods by solving

$$\frac{dI_{ul}}{ds} = -\chi_{ul}(I_{ul} - S_{ul}), \quad (9)$$

where  $I_{ul}$  is the intensity of the line emission from the upper state  $u$  to the lower state  $l$ . The total extinction  $\chi_{ul}$  comes from both dust and gas,

$$\chi_{ul} = \rho_d \chi_\nu + (n_l B_{lu} - n_u B_{ul}) \phi_{ul} \frac{h\nu_{ul}}{4\pi}, \quad (10)$$

and the source function  $S_{ul}$  is given by spontaneous emission and dust emission  $S_\nu$  given in equation (4),

$$S_{ul} = \frac{1}{\chi_{ul}} n_u A_{ul} \phi_{ul} \frac{h\nu_{ul}}{4\pi} + \frac{\rho_d \chi_\nu}{\chi_{ul}} S_\nu. \quad (11)$$

Here,  $n_u$  and  $n_l$  are level populations for the upper and lower state, respectively,  $A_{ul}$ ,  $B_{ul}$ , and  $B_{lu}$  are Einstein coefficients, and  $\phi_{ul}$  is the line profile function. We note that the scattering of line emission by dust particles is not included in this work. Local thermal equilibrium (LTE) is assumed to calculate the level population, which is a valid assumption for lower transition lines of CO in a protoplanetary disk where typical density is much higher than the critical densities for these lines (Pavlyuchenkov et al. 2007). The fractional abundance of  $^{13}\text{CO}$  and  $\text{C}^{18}\text{O}$  is assumed to be  $9 \times 10^{-7}$  and  $1.35 \times 10^{-7}$  (Qi et al. 2011). We have assumed that the line width is determined by thermal broadening.

We construct the model channel maps from  $-4.5 \text{ km s}^{-1}$  to  $4.5 \text{ km s}^{-1}$  with respect to the systemic velocity with  $0.06 \text{ km s}^{-1}$  step and each model channel map is convolved with the Gaussian beam. The model radial profiles of the moments 0 and 1 are then extracted in the north and south directions for comparison with the observations. The continuum emission is subtracted on the image by using line-free channels and the velocity channels showing emission only below the detection limit are excluded when calculating the moment maps from the model. To confirm the validity of continuum subtraction in the image plane, we have also made imaging simulations for several cases in a more rigorous way in which the visibilities for the baselines sampled in our observations are first generated from the disk model with the CASA simulator and then continuum subtraction is made in the  $uv$ -plane. After imaging with the same procedure as that described in section 2.1, we have confirmed that the resultant line profiles agree with those obtained with the image-based continuum subtraction within a few percent.



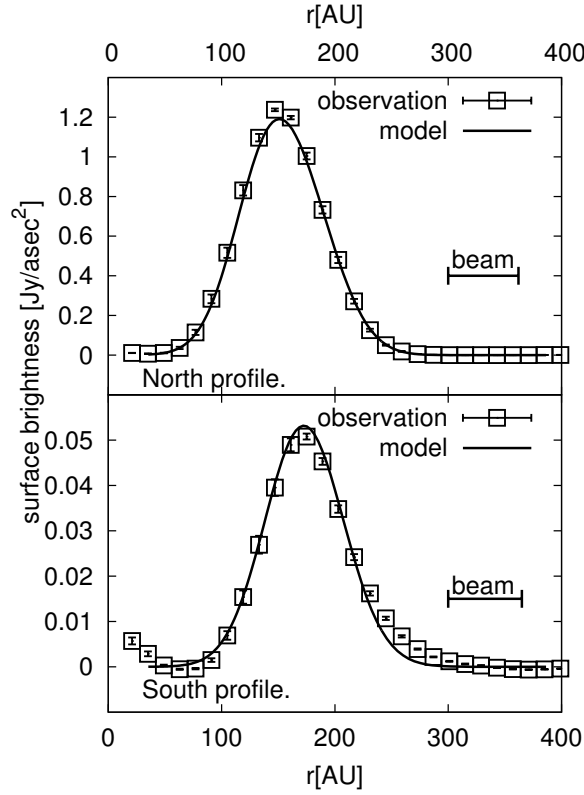


Fig. 7. The comparison of continuum emission and the model surface brightness for the north (top) and south (bottom) profiles.

#### 4 Results of Dust Distribution

We have searched for the parameters  $\Sigma_{d,0}$ ,  $r_d$ , and  $w_d$  in equation (2) that can reproduce the observed north and south profiles. In the south profiles, the parameter search is straightforward since the dust emission is optically thin. In the north, on the other hand, it is necessary to carefully look at the dependence of surface brightness profiles on dust distribution parameters since the dust emission is optically thick (see section 6.2.1). The details of the parameter search for the north profiles are summarized in appendix 2. The best-fit results are summarized in table 2 and figure 7 compares the radial profiles of the dust continuum emissions derived from the model and observations. The best-fit models have the dust density and temperature distributions shown in figure 8. Our derived parameters for the dust disk (or ring) radius and width is consistent with the results of Verhoeff et al. (2011), who show that the massive outer disk extends from 130 AU to 200 AU from the central star based on their modeling of the SED and mid-infrared images (and therefore dust emission).

The dust ring emission is only marginally resolved in ALMA Band 7 since the full width at half maximum (FWHM) of the radial Gaussian function of the model surface density is  $\sim 2\sqrt{\ln 2}w_d \sim 50$  AU (see table 2), which is slightly smaller than the beam size ( $\sim 0''.45 \sim 60$  AU at 140 pc). As a result, the radial width of the observed surface brightness profile ( $\sim 2\sqrt{\ln 2}w_{\text{obs}} \sim 85$  AU in FWHM; see table 1) is larger than that of the model surface density. Perez et al. (2015) measured the radial width of the dust continuum emission at 230 GHz to be  $0''.9$ , while at 345 GHz to be  $\sim 0''.55$ . The difference of the width at different band may be explained by the effect of the convolution by the beam. The radial width of the continuum emission is not well resolved. The ratio of the radial width of the continuum emission between 230 GHz and 345 GHz is  $\sim 1.6$ , which is close to the ratio of the frequency (and thus the ratio of the beam size) between the two bands.

It is indicated that the amount of dust particles is  $\sim 70$  times more at the peak of the north profiles than at the peak of the south profile, although the surface brightness contrast of the dust emission between the north and the south peak locations is  $\sim 24$ . The difference between the surface density contrast and the surface brightness contrast is largely due to the fact that the northern part of the disk is optically thick to dust emission. It should also be noted that the scattered light component in the dust continuum emission is not negligible in the north profile (see section 6.2 for discussion).

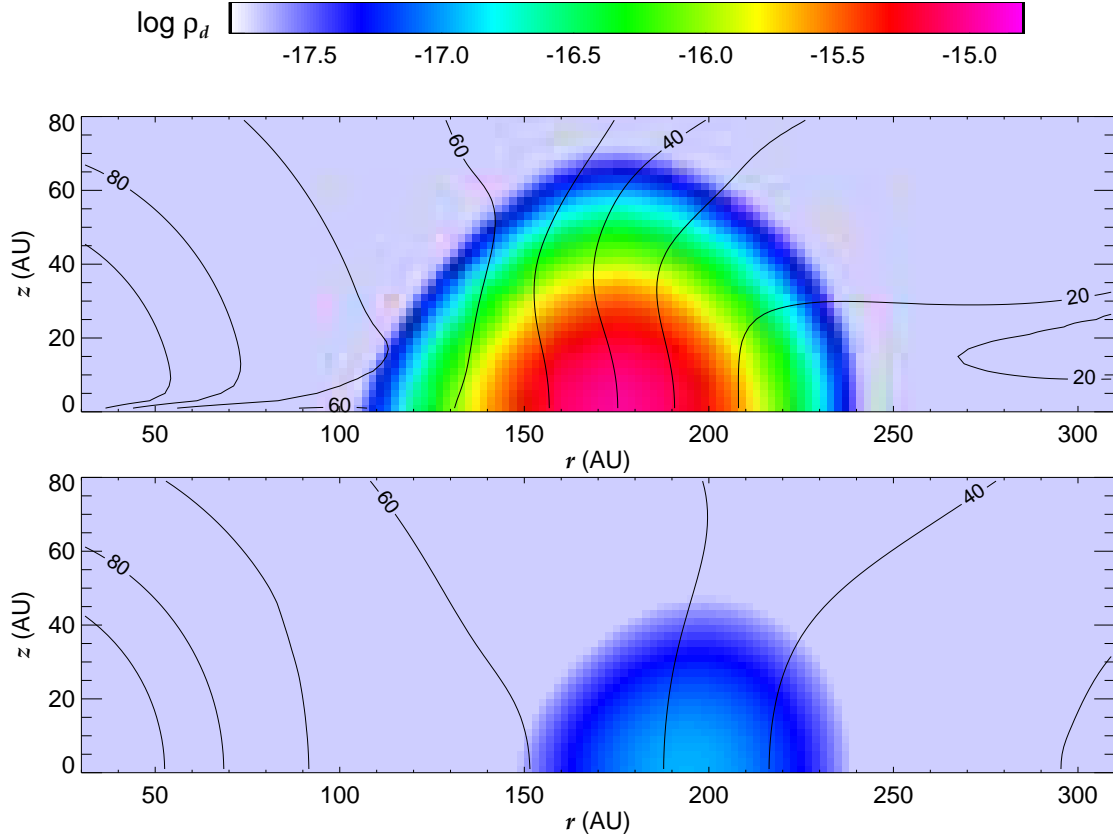


**Fig. 8.** Dust density and temperature distribution for the best-fit models of north (top) and south (bottom) profiles. Gas density is indicated by color in unit of  $\text{g/cm}^3$  and the temperature is shown by contours

	North	South
$\Sigma_{d,0} [\text{g cm}^{-2}]$	0.6	$8.45 \times 10^{-3}$
$r_d [\text{AU}]$	173	196
$w_d [\text{AU}]$	27	34

**Table 2.** Best-fit values for dust distribution.

## 5 Results of Gas Distribution

We now turn our attention to gas distribution. We first show that the models with uniform gas-to-dust ratio 100 do not reproduce the observed profiles in section 5.1. We then describe in detail how we construct the models for gas distribution step by step in subsequent subsections. Our final results are summarized in section 5.6.

### 5.1 Failure of Uniform Gas-to-Dust Ratio Models

We first show that the models with uniform gas-to-dust ratio 100, i.e.,  $\xi(r) = 100$  in equation (6), fail to reproduce the observed radial profiles of moments 0 and 1. In this case, the radial gas surface density profile  $\Sigma_g(r) = \xi(r)\Sigma_d(r)$  is given by a Gaussian function as the dust distribution is. Figure 9 shows the radial profiles of moments 0 and 1 for the north direction and figure 10 shows the same but for the south direction.

At inner radii ( $r \lesssim 100$  AU), the model profiles of moment 0 show too weak emission compared to observations and that of moment 1 tends to be too slow compared to the observations. These indicate that there has to be more gas within 100 AU. On the other hand, around the peak of the dust distribution ( $r \sim 170$  AU for north and  $r \sim 200$  AU for south), the model moment 0 is too bright compared to the observations, especially in the case of  $\text{C}^{18}\text{O}$  profiles. This suggests that gas-to-dust ratio is smaller

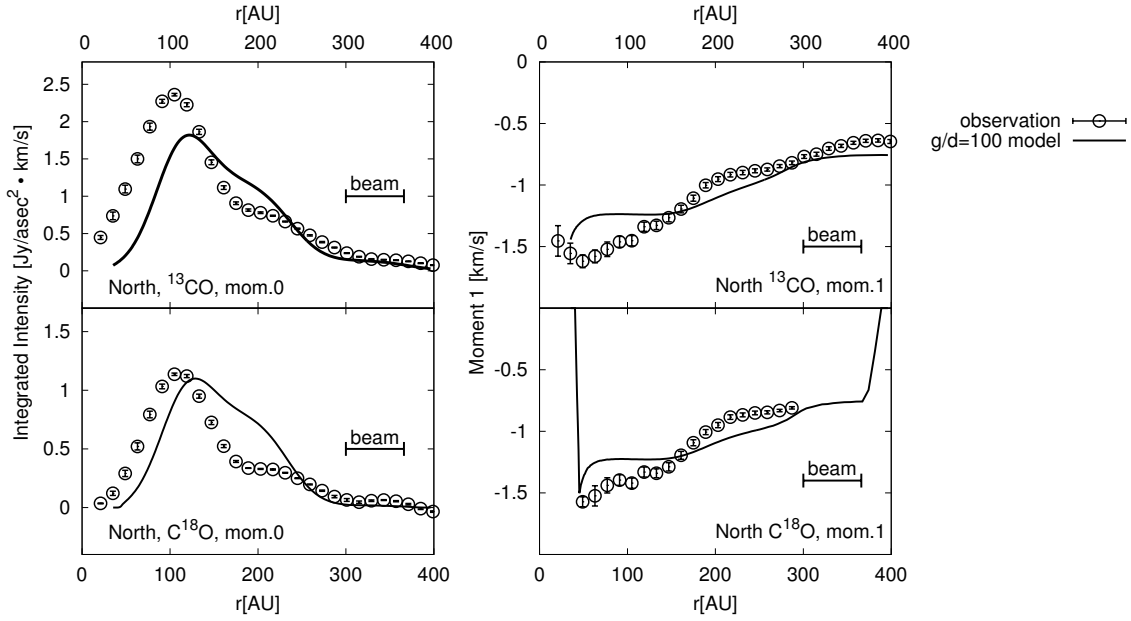


**Fig. 9.** The radial profiles of moment 0 (left panels) and moment 1 (right panels) for  $^{13}\text{CO}$  (top row) and  $\text{C}^{18}\text{O}$  (bottom row) for the north profiles in the case where gas-to-dust ratio is fixed to 100 everywhere in the disk.

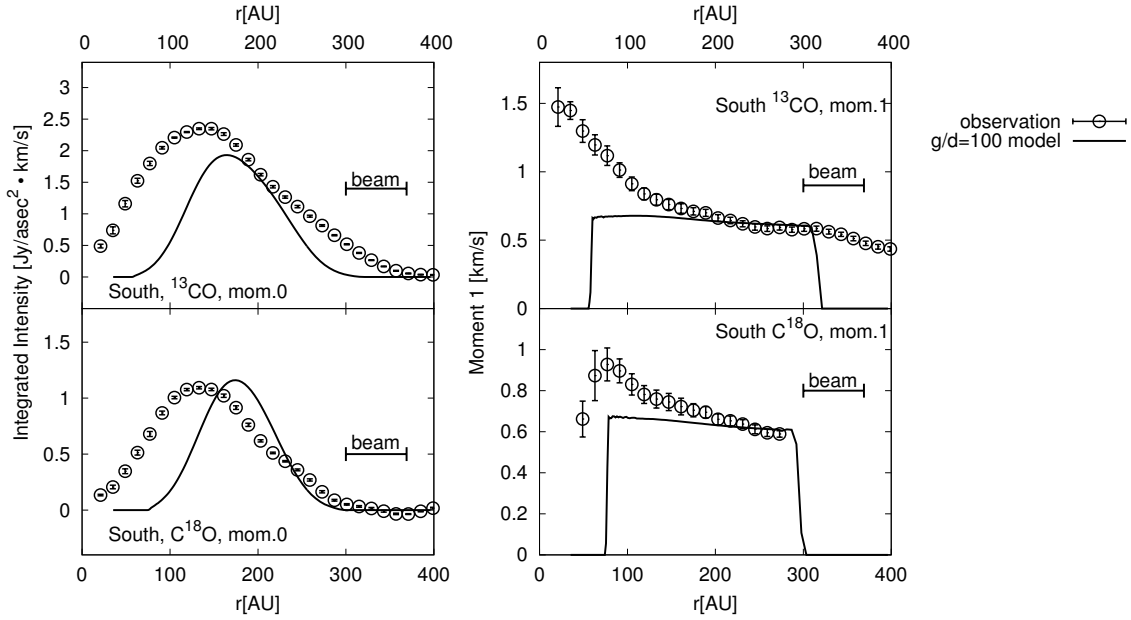


**Fig. 10.** The same as figure 9 but for the south profiles.

$\Sigma_0$ [g/cm <sup>2</sup> ]	0.0845, 0.2325, 0.845, 2.325
$r_c$ [AU]	90, 100, 110, 120
$r_{out}$ [AU]	200, 250, 300, 350

**Table 3.** Parameters explored for power-law gas distribution given by equation (12).

than 100 at places where dust particles are concentrated. It is impossible, however, to decrease the amount of gas at  $\sim 200$  AU and to increase at inner radii simultaneously under the assumption of uniform gas-to-dust ratio. The dust distribution is already determined in section 4. Therefore, we need to consider completely different radial distribution of the gas from the dust by varying the gas-to-dust ratio  $\xi(r)$  within the disk.

## 5.2 Power-Law Gas Profiles

Having found that the uniform gas-to-dust ratio models do not reproduce the observed profiles of gas emission, we now explore models of gas distribution, which is not necessarily restricted to constant gas-to-dust ratio. To acquire consistent results with the dust distribution calculations described in section 3.1, we still assume that the gas-to-dust ratio is constant in the vertical direction *at each radius*, but it is not constant in the radial direction. With a trial function of gas surface density  $\Sigma_g(r)$ , it is possible to calculate the gas-to-dust ratio at each radius by calculating  $\xi(r) = \Sigma_g(r)/\Sigma_d(r)$ , which is then used to obtain the gas density at each grid cell from equation (6).

From the results presented in section 5.1, it is indicated that the gas distribution is more extended in the radial direction than dust. Therefore, we first try the model in which the gas surface density profile  $\Sigma_g(r)$  is given by the  $r^{-1}$  power-law profile at  $r_c < r < r_{out}$ ,

$$\Sigma_g(r) = \Sigma_0 \left( \frac{r}{200 \text{ AU}} \right)^{-1} \quad (r_c < r < r_{out}), \quad (12)$$

and zero otherwise. Here,  $r_c$  can be interpreted as the cavity radius. Since constant gas-to-dust ratio models fail to explain the observed profiles, it is necessary to try models with different gas distribution. The gas-to-dust ratio is not constant in such cases. We have first tried several models with Gaussian surface density profiles with different parameters, but we have found that these models fail to reproduce the observed profiles. This is primarily due to the fact that the gas emission extends to large radii, but Gaussian function falls off too rapidly. Therefore, we consider power-law distribution of the gas surface density, which is more radially extended than Gaussian profiles. We choose power-law distribution as a representative model of such radially extended gas profiles and fix the power-law exponent to  $-1$  in order to reduce the number of free parameters. The choice of  $r^{-1}$  power is motivated by the models of steady state accretion disk, but we do not claim that this is the only possible solution. We aim to find one possible disk model that reasonably reproduces observations and discuss its implications for the overall picture of how the dust and gas are distributed.

We explore the parameter space of  $(\Sigma_0, r_c, r_{out})$  and look for values that match the observed moments 0 and 1 profiles for the north and south profiles. Our strategy is to find first the values of  $\Sigma_0$  that reasonably matches with the observations at  $150 \text{ AU} \lesssim r \lesssim 200 \text{ AU}$ , where dust emission is bright. Then we look for the values of  $r_c$  by investigating the inner radii. Finally, we search for the values of  $r_{out}$  by investigating the outer radii. We show the results one by one in subsequent sections. The values of these three parameters explored in our set of calculations are summarized in table 3.

## 5.3 The Overall Gas Distribution

We first find the values of  $\Sigma_0$  that reasonably match the observed profiles at  $150 \text{ AU} \lesssim r \lesssim 250 \text{ AU}$ . For this purpose, we fix  $(r_c, r_{out}) = (100 \text{ AU}, 280 \text{ AU})$  for both north and south profiles and we vary  $\Sigma_0$  from  $0.0845 \text{ g cm}^{-2}$  to  $2.325 \text{ g cm}^{-2}$  with a step of a factor of  $\sim 3$  (see table 3 for specific parameters). The lowest value of  $\Sigma_0$  is chosen in such a way that the gas-to-dust ratio at the peak of the dust distribution in the south direction is 10. Figures 11 and 12 show the results for the north and south profiles, respectively.

For the north profiles of  $\text{C}^{18}\text{O}$  moment 0, the observations fall between the models with  $\Sigma_0 = 0.845 \text{ g cm}^{-2}$  and  $\Sigma_0 = 2.325 \text{ g cm}^{-2}$ . For  $\text{C}^{13}\text{O}$  moment 0, the model with  $\Sigma_0 = 2.325 \text{ g cm}^{-2}$  seems to show better fit, but it is actually difficult to judge which is plausible when the existence of remaining gas inside the cavity is considered (see section 5.4). Note that all the models fail to explain the moment 0 profile within the cavity ( $r < r_c = 100 \text{ AU}$ ) as the model profiles fall off too rapidly towards inner radii. This is because there is no gas emission inside 100 AU in the model. We also point out that the model moment 1 profiles show too slow velocity at inner radii. This is because moment 1 is calculated to be zero in such gas-free regions before we convolve

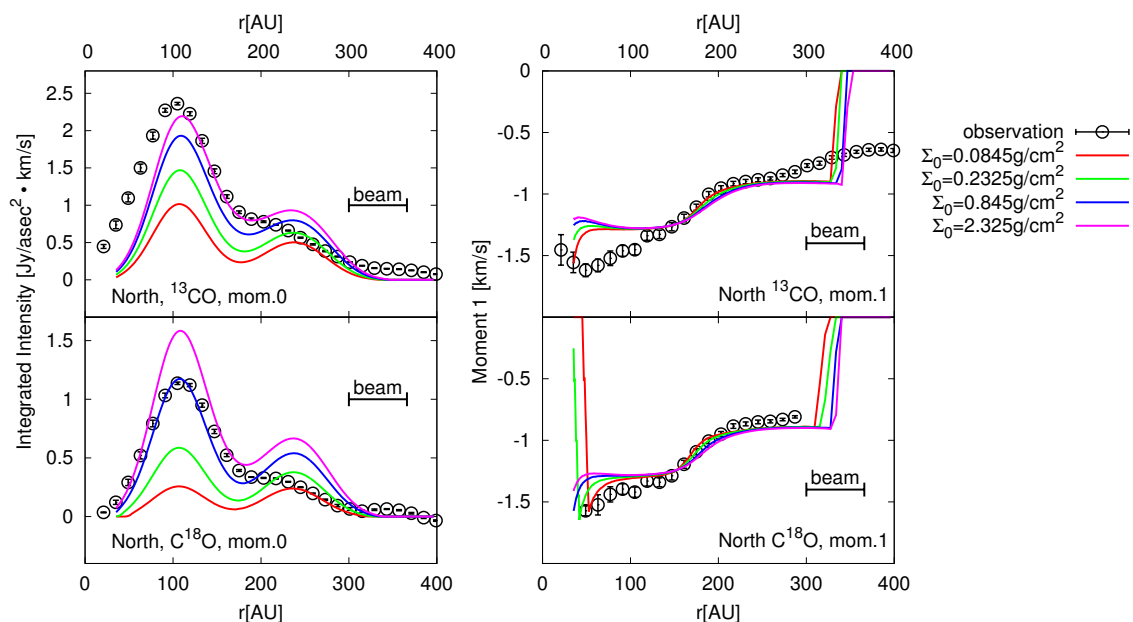


Fig. 11. The radial profiles of moment 0 (left panels) and moment 1 (right panels) for  $^{13}\text{CO}$  (top row) and  $\text{C}^{18}\text{O}$  (bottom row) for the north direction when the parameter  $\Sigma_0$  is varied.

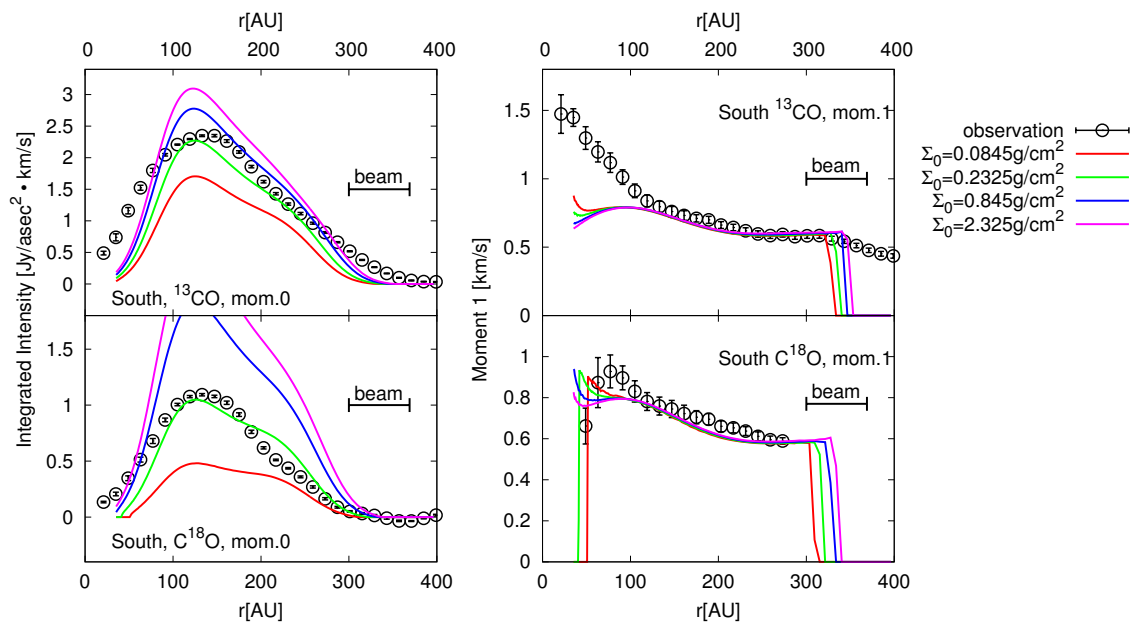


Fig. 12. The same as figure 11 but for the south profiles.

the model with the beam. The apparent emission inside the cavity in the model is the result of beam dilution. Similar discrepancy between the model and observations can be found at the outer radii of  $r \gtrsim 300$  AU, while in this case the beam dilution is not as significant as inner radii.

One prominent feature of the model north profile is the two peaks of the surface brightness profiles at  $r \sim 100$  AU and  $r \sim 250$  AU, while the gas surface density profile is smooth. These peaks are primarily due to the existence of large amount of dust in relatively narrow radial range. The dust emission is optically thick and is very bright. The line emission is partially hidden by the optically thick dust. Therefore, the difference in brightness between dust continuum and line emissions is not very significant. The line emission at the peak of the dust emission is largely affected when the continuum emission is subtracted to calculate moment maps. The two “peaks” of gas emission should be considered as “one trough” caused by the subtraction of bright continuum emission. Although not as prominent as the model profiles, it is possible to see this effect in the observed profiles, which show a slight dip of the moment 0 at  $\sim 170$  AU (see figure 5 and 11). We further discuss about these apparent bump and/or trough structures in section 6.3.

For the south profiles,  $\Sigma_0 = 0.2325 \text{ g cm}^{-2}$  models show reasonable fit to both  $^{13}\text{CO}$  and  $\text{C}^{18}\text{O}$ . However, the discrepancy between the model moment 1 profiles and the observations at inner and outer radii is present, as in the north profile case. This discrepancy is further studied in sections 5.4 and 5.5. We note that the “trough” structure is not very significant in the south profile since the continuum emission is weak and the continuum level is sufficiently low. Comparing the values of  $\Sigma_0$  derived for the south profile with that for the north, it is indicated that the azimuthal asymmetry of gas distribution is not as significant as dust distribution. The azimuthal contrast of gas surface density is only by a factor of  $\sim 3 - 10$  between the north and south profiles, while the peak dust surface density differs by a factor of  $\sim 70$ .

#### 5.4 Inner Radius of the Gas and Remaining Gas inside Cavity

We now explore the parameter space for  $r_c$ , the cavity radius of the gas. We fix  $(\Sigma_0, r_{\text{out}}) = (0.845 \text{ g cm}^{-2}, 280 \text{ AU})$  and  $(\Sigma_0, r_{\text{out}}) = (0.2325 \text{ g cm}^{-2}, 280 \text{ AU})$  for the north and south profiles, respectively. We vary  $r_c$  from 90 AU to 120 AU, and see whether we can match the observed profiles within  $r \lesssim 150$  AU. Especially, we look for values of  $r_c$  which matches the peak locations of the moment 0 profiles residing at  $r \sim 110$  AU in the north profile and at  $r \sim 140$  AU in the south profile.

Figures 13 and 14 show the results for the north and south profiles, respectively. It is shown that  $r_c \sim 100 - 110$  AU can explain the location of the peak in the profiles of moment 0. However, all the models give slower velocity in moment 1 profile than observations at  $r \lesssim 100$  AU. It should also be noted that the model profiles of moment 0 fall to zero quickly towards the inner radii while the observed profiles, especially  $^{13}\text{CO}$  south profiles, show more gradual decrease.

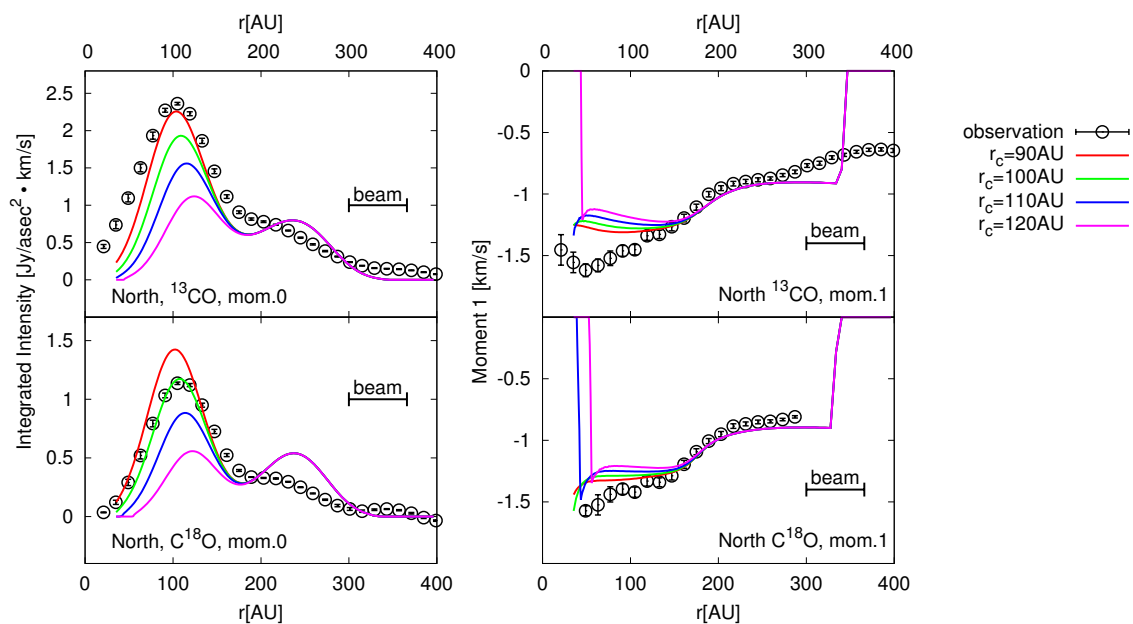
The discrepancy between the model and observed profiles at inner radii can be explained if we assume that there is some remaining gas at  $r < r_c$ . The existence of gas inside the cavity is also indicated by the existence of  $^{12}\text{CO}$  emission all the way to the central star (Casassus et al. 2013; Rosenfeld et al. 2014; Perez et al. 2015). To explore the parameters, we assume that the gas surface density at  $r < r_c$  is given by

$$\Sigma_g(r) = f_{\text{in}} \Sigma_g(r_c) \left( \frac{r}{r_c} \right) \quad (r < r_c) \quad (13)$$

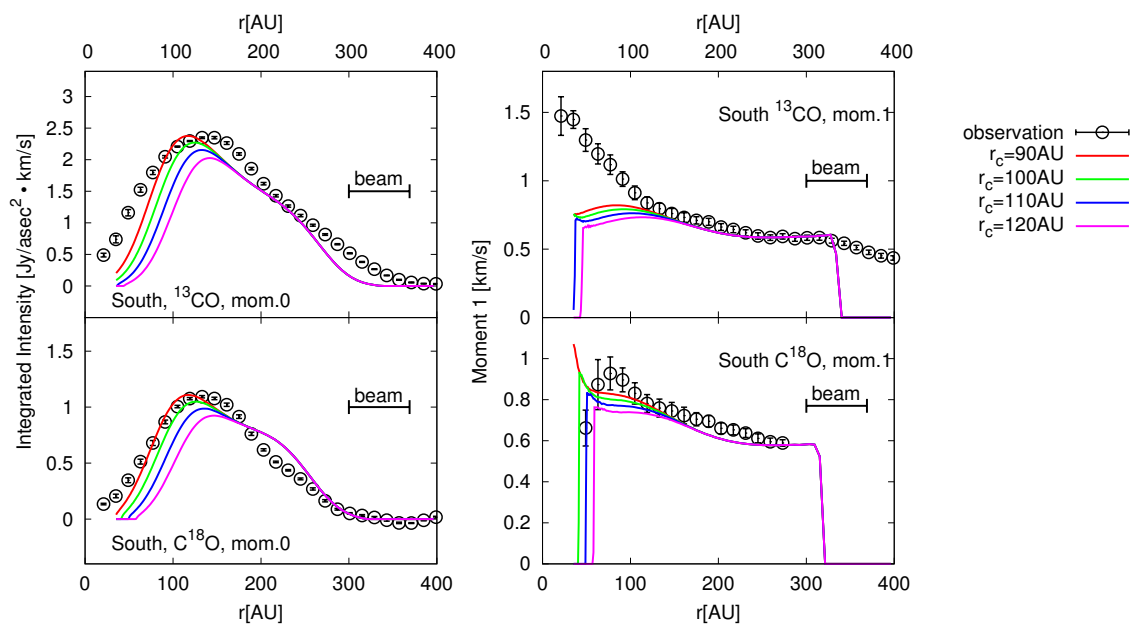
while the gas at  $r > r_c$  is kept the same as equation (12). The parameter  $f_{\text{in}}$  is varied from 0 (complete cavity) to  $3/16$  for the north models and from 0 to  $3/8$  for the south models (see table 4). Figures 15 and 16 show the results for the north and south profiles, respectively. It is clear that the match between the model and observations is better for the models with remaining inner gas. The values of  $f_{\text{in}}$  that give the best match between the model and observations seem to be  $\sim 1/8$  for the south profile. For the north model, the best-fit lies somewhere between  $1/16$  and  $1/8$ . To keep the parameter search simple, we allow a factor of  $\sim 2$  error here, and use  $1/8$  as a representative value. An important indication from the modeling approach is that similar gas distribution models (within a factor of  $2 - 3$ ) can account for the observations both in the north and south regions of the disk, which is very different from the case of dust distribution.

We have assumed that the gas surface density increases linearly with radius within  $r < r_c$ . However, the functional form of the gas distribution does not affect the results. We have checked this by using a series of models with constant gas surface density at  $r < r_c$ . This is partly because the beam size is relatively large and the beam dilution effect is significant especially when we discuss the gas distribution at inner radii. We therefore conclude that it is a robust conclusion that there should be some remaining gas within the cavity but there is an uncertainty in the details of how the gas is distributed. Indeed, Perez et al. (2015) have used different functional form for the models of gas inside the cavity and obtained results consistent with observations. The amount of gas within



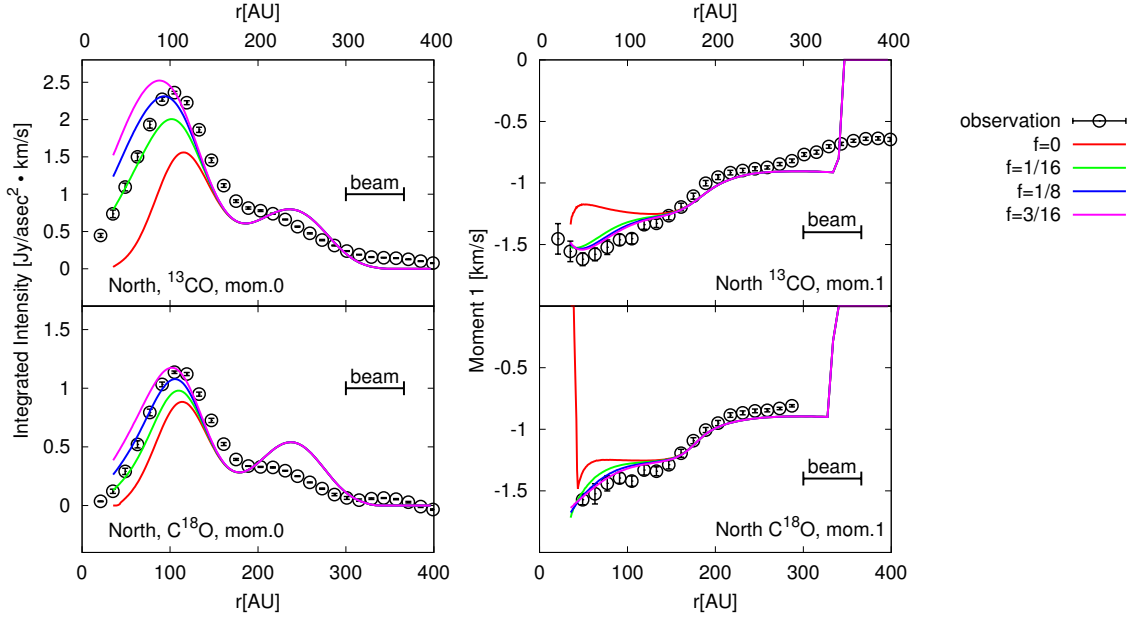


**Fig. 13.** The radial profiles of moment 0 (left panels) and moment 1 (right panels) for  $^{13}\text{CO}$  (top row) and  $\text{C}^{18}\text{O}$  (bottom row) for the north direction when the parameter  $r_c$  is varied.



**Fig. 14.** The same as figure 13 but for the south profiles.

$\Sigma_0$ [g cm <sup>2</sup> ] (north)	0.845	$\Sigma_0$ [g/cm <sup>2</sup> ] (south)	0.2325
$r_c$ [AU] (north)	110	$r_c$ [AU] (south)	100
$r_{\text{out}}$ [AU]	280	$r_{\text{out}}$ [AU]	280
$f_{\text{in}}$ (north)	0, 1/16, 1/8, 3/16	$f_{\text{in}}$ (south)	0, 1/8, 1/4, 3/8

**Table 4.** Parameters explored for remaining gas inside cavity**Fig. 15.** The radial profiles of moment 0 (left panels) and moment 1 (right panels) for <sup>13</sup>CO (top row) and C<sup>18</sup>O (bottom row) for the north direction when the parameter  $f_{\text{in}}$  is varied.

the cavity in Perez et al. (2015)<sup>4</sup> is  $\sim 1 - 2 \times 10^{-3} M_{\odot}$  while we have the gas mass inside the cavity being  $\sim 5 \times 10^{-4} M_{\odot}$  if we integrate the model with  $(\Sigma_0, r_c, f_{\text{in}}) = (0.845 \text{ g/cm}^2, 110 \text{ AU}, 1/8)$ , which is preferred for the north profile, from  $r = 0$  to  $r = r_c$ . These results are consistent within an order of magnitude. We consider that the difference comes from the fact that they use lower temperature and smaller line width than our model in estimating the gas mass inside the cavity (see also section 6.2.3).

### 5.5 Outer Radius of Dense Gas and Remaining Tenuous Gas at Large Radii

We now turn our attention to the gas distribution at outer radii. In the series of models presented in sections 5.3 and 5.4, the outer radius of the gas distribution is fixed to  $r_{\text{out}} = 280 \text{ AU}$ . As indicated in figures 11-14, the moment 1 radial profiles of <sup>13</sup>CO cuts off at  $\sim 350 \text{ AU}$  while the observations indicate that there must be some gas at outer radii.

To explore the parameter space, we first vary  $r_{\text{out}}$  while keeping  $(\Sigma_0, r_c, f_{\text{in}}) = (0.845 \text{ g/cm}^2, 110 \text{ AU}, 0)$  and  $(\Sigma_0, r_c, f_{\text{in}}) = (0.2325 \text{ g/cm}^2, 100 \text{ AU}, 0)$  for the north and south models, respectively. We have checked that the details of the choice of  $r_c$  and  $f_{\text{in}}$  does not affect the brightness profiles at outer radii. Figures 17 and 18 show the results for the north and south profiles, respectively. It is shown that the moment 1 profiles indeed extend to larger radii as we increase  $r_{\text{out}}$ . However, if  $r_{\text{out}}$  exceeds 250 AU, the models show much larger values of moment 0 than observed at outer radii.

The discrepancy of the moment 0 profiles between the observations and models indicates that we need to decrease the amount of gas at outer radii than currently assumed power-law profiles, especially at  $r > 250 \text{ AU}$ . At the same time, there should still be some gas remaining at outer radii so that moment 1 profiles do not cut off. As an alternative series of models, we now try commonly used exponential taper model given by

$$\Sigma_g(r) = \Sigma_0 \left( \frac{r}{200 \text{ AU}} \right)^{-1} \exp \left( -\frac{r}{r_{\text{out}}} \right) \quad (14)$$

<sup>4</sup> The cavity radius is 90 AU in their model

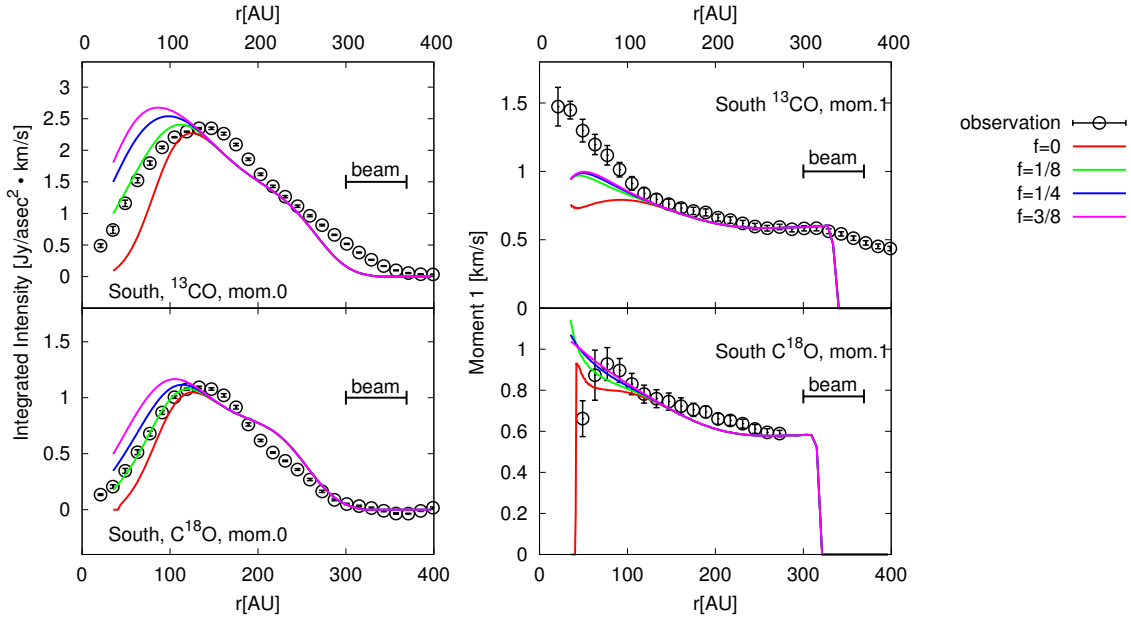


Fig. 16. The same as figure 15 but for the south profiles.

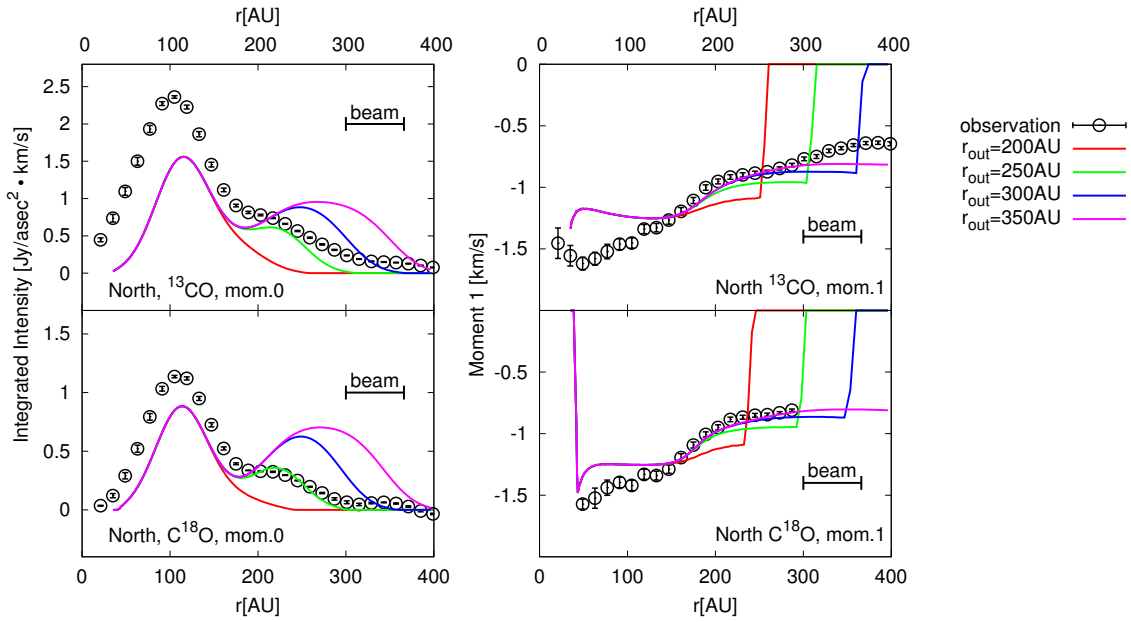


Fig. 17. The radial profiles of moment 0 (left panels) and moment 1 (right panels) for  $^{13}\text{CO}$  (top row) and  $\text{C}^{18}\text{O}$  (bottom row) for the north direction when the parameter  $r_{\text{out}}$  is varied. For this parameter search, we assume that there is no gas outside  $r_{\text{out}}$ .

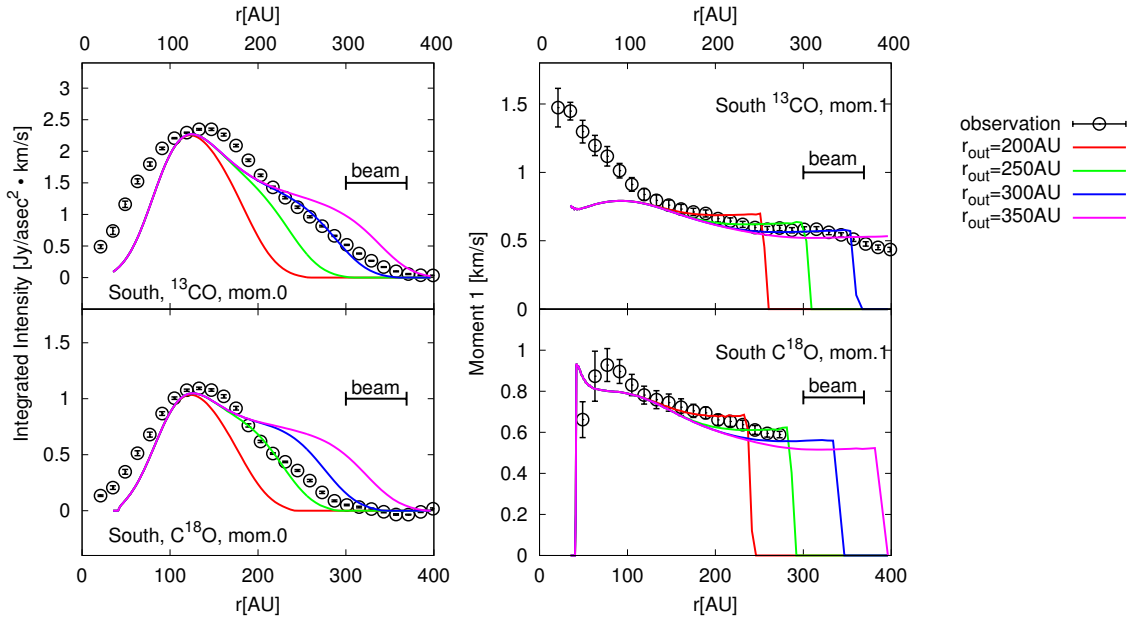


Fig. 18. The same as figure 17 but for the south profiles.

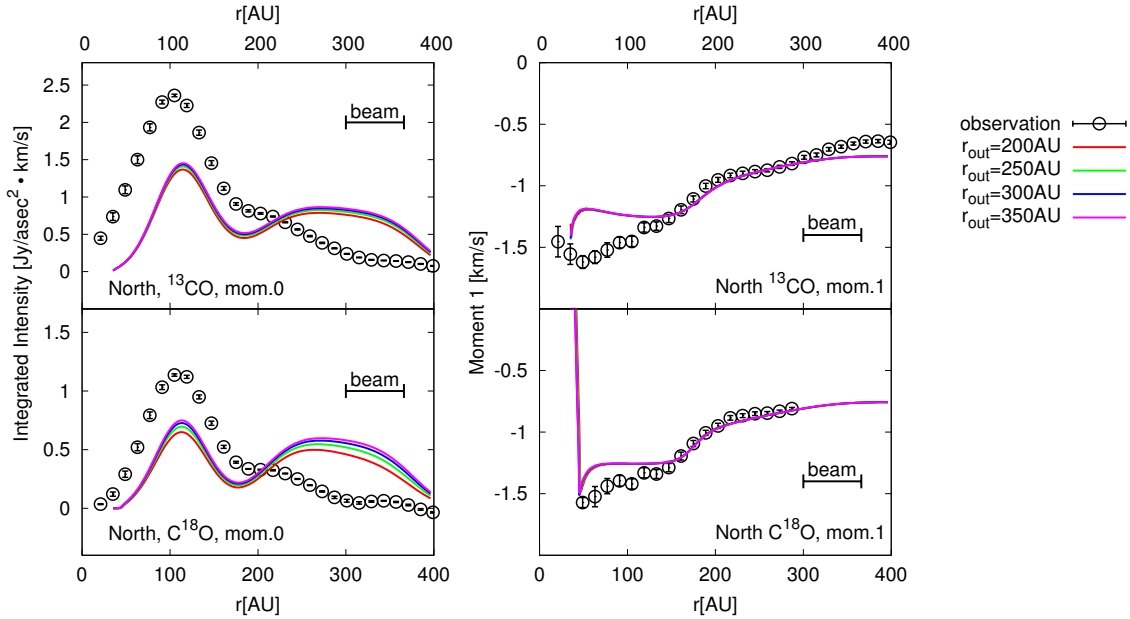


Fig. 19. The radial profiles of moment 0 (left panels) and moment 1 (right panels) for  $^{13}\text{CO}$  (top row) and  $\text{C}^{18}\text{O}$  (bottom row) for the north direction when the parameter  $r_{\text{out}}$  is varied. For this parameter search, we assume that the gas at outer radii exhibits exponential cutoff as in equation (14).

for  $r > r_c$ . The results are shown in figures 19 and 20 for the north and south profiles, respectively. Although the model moment 1 profiles show good match with observations for both the north and south profiles, the models still exhibit too large values for the moment 0 profiles. This indicates that the gas surface density should decrease more rapidly than exponential profiles at outer radii.

To incorporate the rapid decrease of gas surface density at outer radii, we finally try a series of model gas surface density profiles that cut off at  $r_{\text{out}} = 250$  AU but there is remaining, tenuous gas with constant surface density at  $r > r_{\text{out}}$  all the way to the outer edge of the computational domain. In this framework, the gas surface density at  $r > r_{\text{out}}$  is given by

$$\Sigma_{g,\text{out}}(r) = f_{\text{out}}\Sigma_g(r_{\text{out}}) \quad (r > r_{\text{out}}), \quad (15)$$

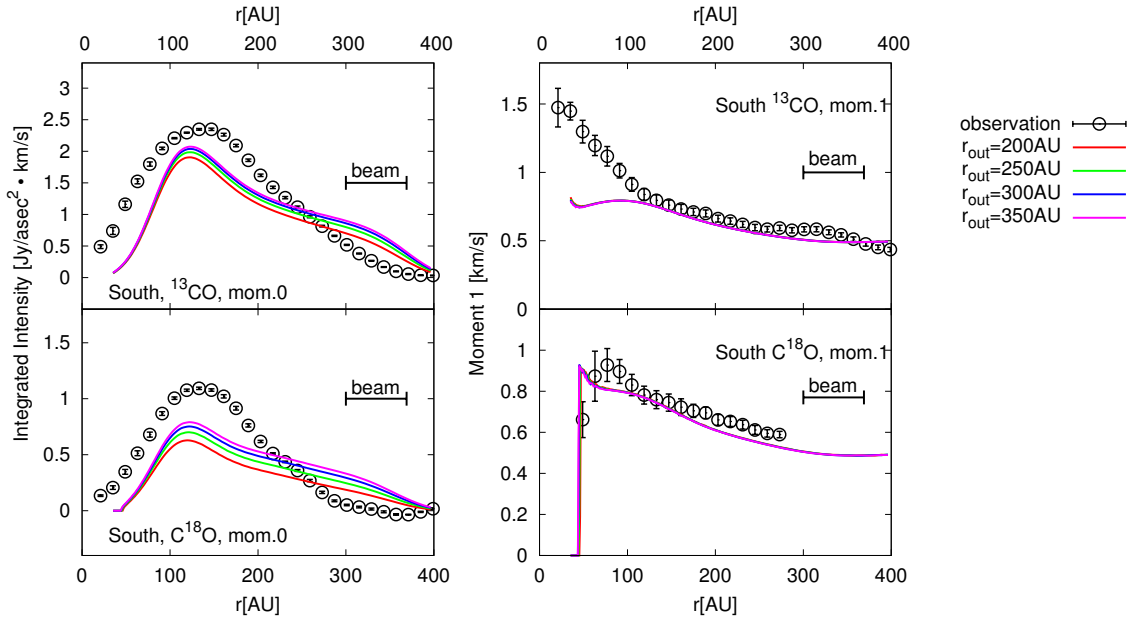


Fig. 20. The same as figure 19 but for the south profiles.

$\Sigma_0$ [g/cm <sup>2</sup> ] (north)	0.845	$\Sigma_0$ [g/cm <sup>2</sup> ] (south)	0.2325
$r_c$ [AU] (north)	110	$r_c$ [AU] (south)	100
$r_{out}$ [AU]	250	$r_{out}$ [AU]	250
$f_{out}$	$1, 10^{-1}, 10^{-2}, 10^{-3}$	$f_{out}$	$1, 10^{-1}, 10^{-2}, 10^{-3}$

Table 5. Parameters explored for tenuous gas outside

where  $\Sigma_g(r_{out})$  is the surface density at  $r = r_{out}$  given by the power-law distribution in equation (12) and  $f_{out}$  controls the amount of remaining gas at outer radii. The parameters explored are given in table 5.

Figures 21 and 22 show the results for the north and south profiles, respectively. For the north profiles, the model profiles at  $r \gtrsim 250$  AU show reasonable match with observations when  $f_{out} \sim 10^{-2}$ . For the south profiles,  $f_{out} = 10^{-1}$  models show agreement at  $r \lesssim 300$  AU while they show brighter emission than observations at the outermost radii. The moment 0 profiles of the model with  $f_{out} = 10^{-2}$  is fainter than observations all the way in the outer radii. Therefore, the actual values of  $f_{out}$  may vary as a function of radius for the south profiles, but the overall value of  $f_{out}$  may be around  $\sim 10^{-1}$  to  $\sim 10^{-2}$ . Finally, we briefly note that the appearance of the “trough” at  $r \sim 170$  AU in the north profile (see discussions in section 5.3) is different when we use different profiles at  $r \gtrsim r_{out}$ . This is because the change in gas surface density at outer radii (within the parameters explored in this section) mainly affects the moment 0 profiles at  $r \gtrsim 200$  AU. The strength of the second (apparent) bump at  $r \sim 250$  AU is therefore affected.

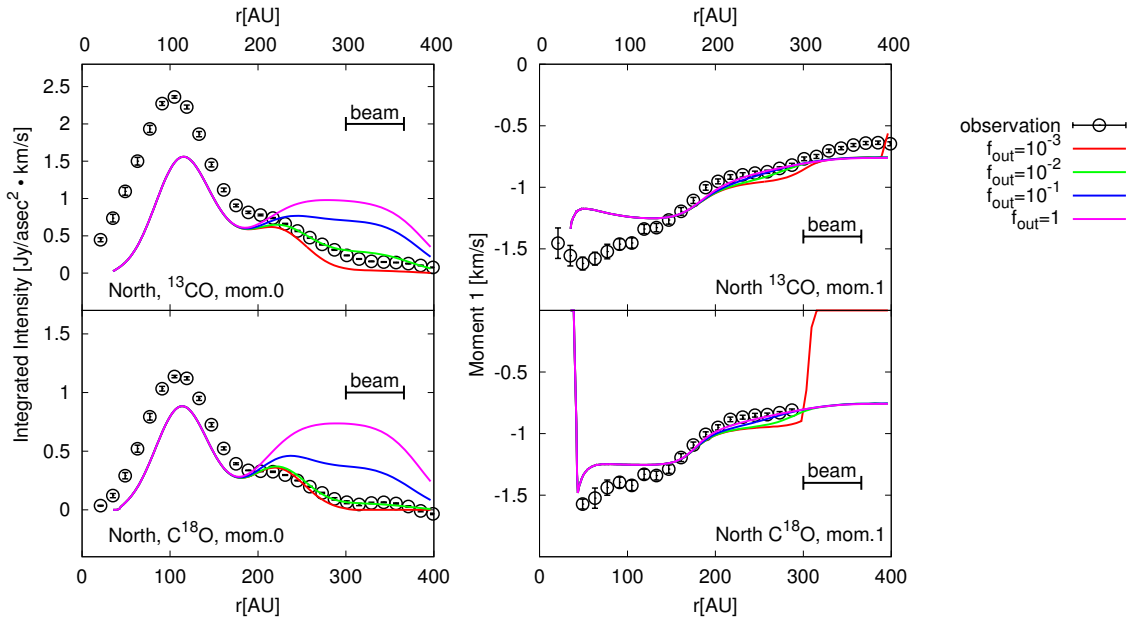
## 5.6 Summary of Gas Distribution

We have looked for the gas distribution models that reproduce the observed moments 0 and 1 profiles of  $^{13}\text{CO}$  and  $\text{C}^{18}\text{O}$ . We have shown that the gas-to-dust ratio is not constant in the disk and that the gas distribution should be more extended in the radial directions than the dust distribution. We have seen that there should be some remaining gas inside  $\sim 100$  AU and some tenuous gas at  $r \gtrsim 250$  AU.

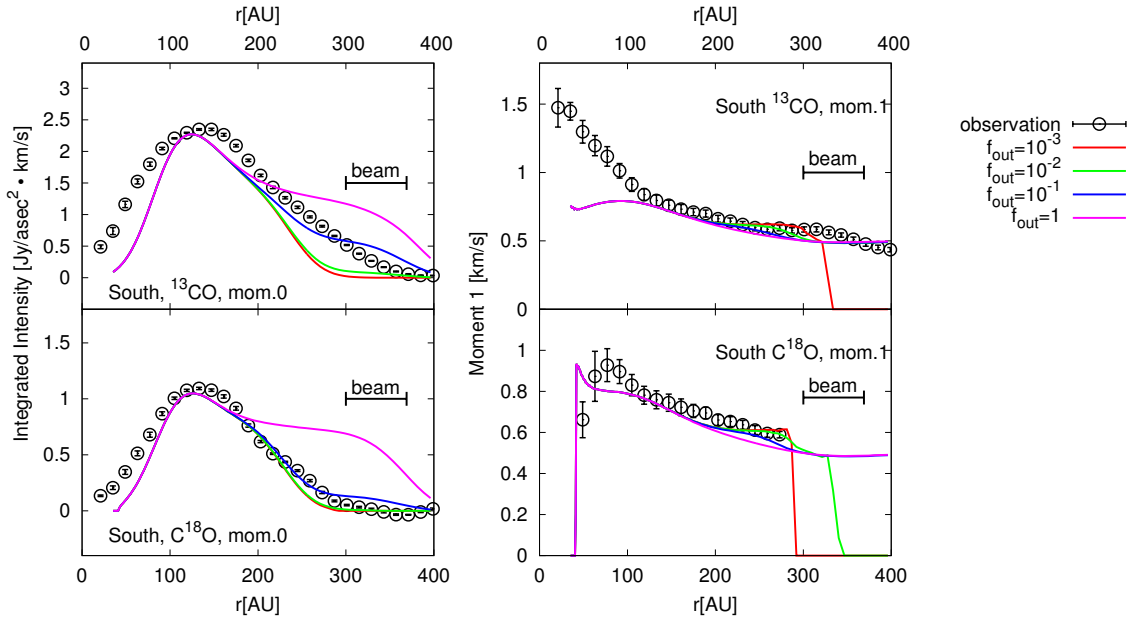
To be more specific, we have assumed that the model surface density of gas is given by

$$\Sigma_g(r) = \begin{cases} f_{in}\sigma(r_c)\left(\frac{r}{r_c}\right) & (r < r_c) \\ \sigma(r) & (r_c < r < r_{out}) \\ f_{out}\sigma(r_{out}) & (r > r_{out}) \end{cases}, \quad (16)$$

where  $\sigma(r)$  is given by the power-law distribution,



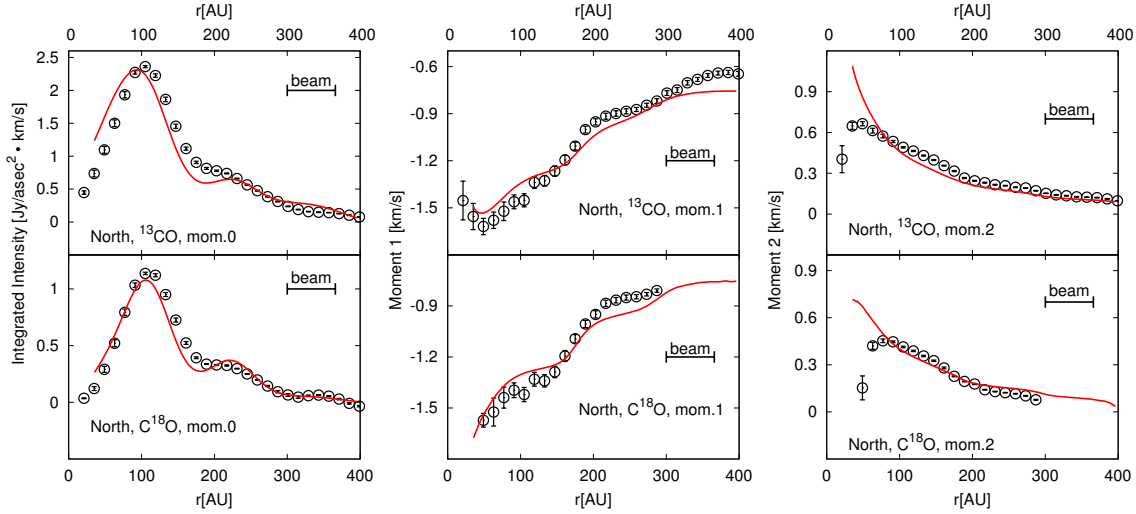
**Fig. 21.** The radial profiles of moment 0 (left panels) and moment 1 (right panels) for  $^{13}\text{CO}$  (top row) and  $\text{C}^{18}\text{O}$  (bottom row) for the north direction when the parameter  $f_{\text{out}}$  is varied. For this parameter search, we assume that the gas at outer radii exhibits a cutoff at 250 AU, but there is still some remaining gas outside the cutoff radius as in equation (15).



**Fig. 22.** The same as figure 21 but for the south profiles.



	North	South
$\Sigma_0$ [ $\text{g cm}^{-2}$ ]	0.845	0.2325
$f_{\text{in}}$	1/8	1/8
$r_c$ [AU]	110	100
$r_{\text{out}}$ [AU]	250	250
$f_{\text{out}}$	$10^{-2}$	$10^{-1}$

**Table 6.** Parameters of the reference models for gas distribution.**Fig. 23.** North radial profiles of moment 0 (left panels), moment 1 (middle panels), and moment 2 (right panels) of  $^{13}\text{CO}$  (top row) and  $\text{C}^{18}\text{O}$  (bottom row) for the reference model given by equation (16). The values of the model parameters are given in table 6.

$$\sigma(r) = \Sigma_0 \left( \frac{r}{200 \text{ AU}} \right)^{-1}. \quad (17)$$

There are five control parameters:  $\Sigma_0$  that determines the overall amount gas surface density,  $r_c$  that determines the inner cutoff (cavity) radius,  $f_{\text{in}}$  that determines the amount of gas within the cavity,  $r_{\text{out}}$  that determines the outer radius of the disk, and  $f_{\text{out}}$  that determines the amount of tenuous gas at large radii. The values of these parameters that give reasonable fit to observations are given in table 6. Hereafter, we call these best-fit models “reference models”.

The comparison of the radial profiles between the models and observations is given in figures 23 and 24 for the north and south directions, respectively. For these models, we show the comparison between the models and observations of the moment 2 radial profiles averaged over  $11^\circ \leq PA \leq 33^\circ$  (north) and  $211^\circ \leq PA \leq 233^\circ$  (south) as well as the moments 0 and 1, which have been the main focus of the modeling. The radial profiles of all the moments show reasonable match between observations and models. Finally, we show the comparison of P-V diagrams in the north and south directions for the reference models in figure 25. The models and observations show reasonable match not only in the radial profiles of the moment maps but also in the P-V diagram.

The radial profiles of the model moment 0 profiles exhibit some bumps and troughs while observations show more smooth profiles. This is most prominent at around  $\sim 170 - 200$  AU region of the north profiles where the dust emission is very bright. These bumps are apparent structures due to the subtraction of bright continuum emission, and we discuss about this further in section 6.3.

## 6 Discussions on the Reference Model

We have constructed the models of dust and gas distribution in the protoplanetary disk around HD 142527. In this section, we look at our reference models of dust and gas distribution and discuss indications and caveats of our model.

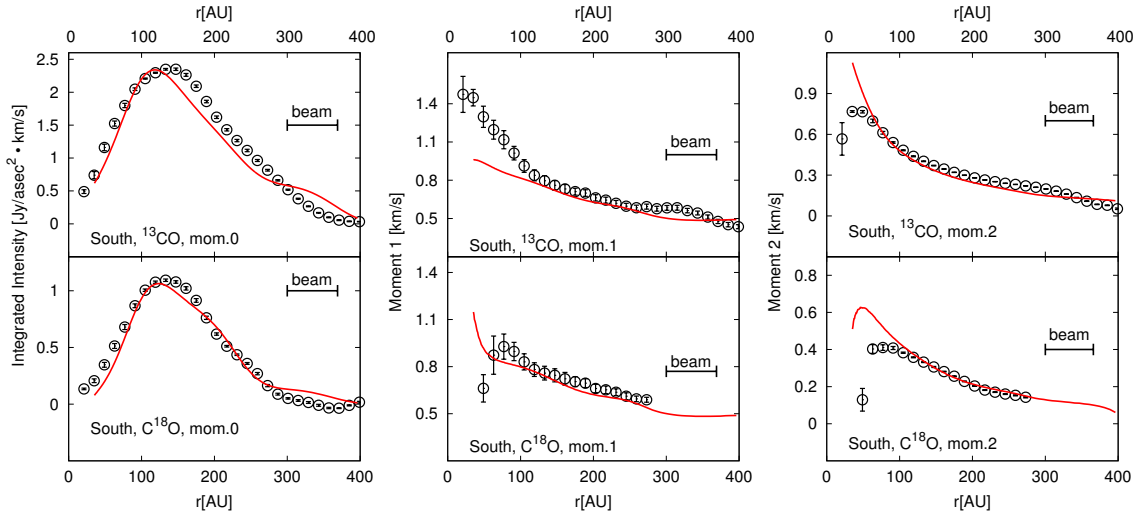


Fig. 24. The same as figure 23 but for the south profiles.

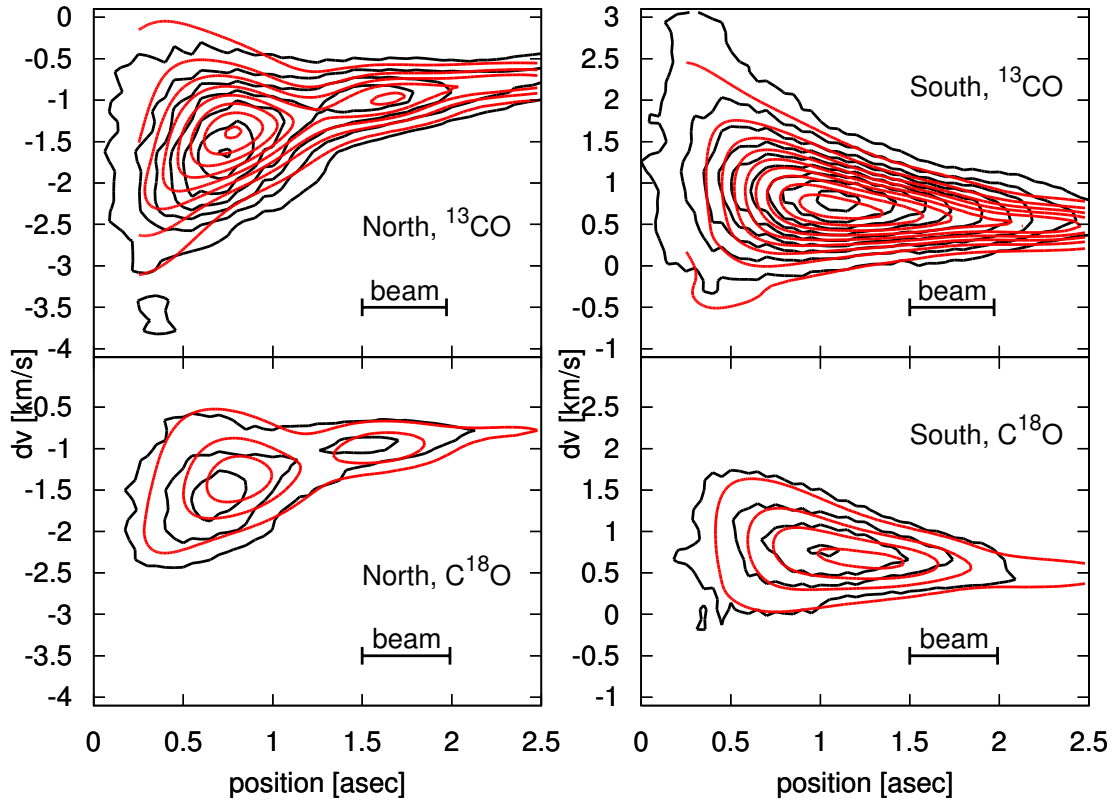
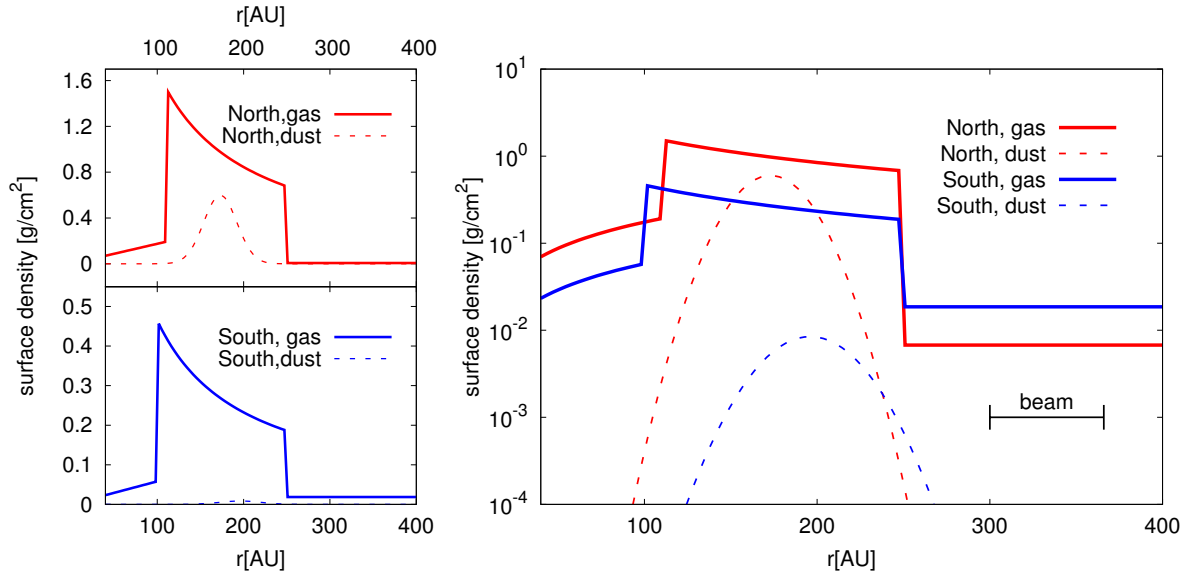


Fig. 25. Comparison of P-V diagram between observations (black contours) and the model (red contours) for the north and south directions. The left panels show the north direction and the right panels show south direction, while the top row shows the results for  $^{13}\text{CO}$  and the bottom row shows  $\text{C}^{18}\text{O}$ . Contours start from  $5\text{-}\sigma$  level ( $0.135 \text{ Jy/asec}^2$  for  $^{13}\text{CO}$  and  $0.175 \text{ Jy/asec}^2$  for  $\text{C}^{18}\text{O}$ , respectively) with  $10\text{-}\sigma$  step.



**Fig. 26.** Surface density distribution of gas (solid line) and dust (dashed line) in northern (red) and southern (blue) part of the disk. The left panels show surface density in the linear scale (top panel for the north and the bottom panel for the south model), while the right panel shows the surface density in the log scale.

### 6.1 Summary of Gas and Dust Distribution

We have shown that the gas and dust are distributed very differently in the disk. Figure 26 shows the surface density profiles of gas and dust in the north and the south regions for the reference model. Dust distribution can be explained by the radial Gaussian ring-like profile with the width of  $w_d \sim 30$  AU (50 AU in FWHM) for both the northern and southern regions. However, there is a factor of  $\sim 70$  difference in surface density between the two regions (see equation (2) and parameters listed in table 2 for dust distribution). Gas distribution is more or less axisymmetric and radially extended. The variation of surface density between the northern and southern part is a factor of  $\sim 3$  and the gas density cuts off at  $r_c \sim 100$  AU, and  $r_{\text{out}} \sim 250$  AU, but both inner and outer regions are not completely devoid of gas (see equation (16) and parameters listed in table 6 for gas distribution).

The gas-to-dust ratio is  $\sim 30$  at the peak of the dust emission in the southern part of the disk, while it reaches  $\sim 3$  in the northern peak. Since dust emission is optically thick in the northern part of the disk, the dust emission is not very sensitive to the amount of dust (see appendix 2) so the amount of dust in the northern part may be considered as a lower limit. Therefore, the gas-to-dust ratio may be even lower in the northern part of the disk. The gas-to-dust ratio significantly lower than the canonical value (100 in the ISM) in the northern part indicates that the disk surface density (dust+gas) is not high enough to collapse into a protoplanet by gravitational instability (Fukagawa et al. 2013).

The radial distributions of dust and gas are fixed to Gaussian and power-law (with modifications at inner and outer radii) functions, respectively, in our modeling. The parameters that give a reasonable fit to observations are searched manually. Our model is one of the solutions but not unique, and we consider that the numbers listed in table 6 have at least a factor of  $\sim 2$  uncertainties, especially for  $\Sigma_0$ . It is difficult to constrain the radial distributions more definitely since the spatial resolution is limited. Still, we can argue that the gas distribution is more extended in the radial direction than dust and the gas-to-dust ratio is lower in the north than south.

At a glance at figure 26, the gas distribution may be interpreted as “radially extended bump” and the dust particles are strongly accumulated in this bump region. Although the locations of the peak of the continuum emission and gas moment 0 profiles are different in the observed profiles (see figure 5), our model indicates that the peak of dust surface density profiles is within the region of gas surface density bump, which is between  $r \sim 100$  AU and  $r \sim 250$  AU. The peak of the gas emission at  $\sim 100$  AU is partially due to the fact that the gas temperature is higher at inner radii. Interestingly, the bump in gas seems to be weaker in the south region than in the north. Such distribution of dust and gas seems to be, at least qualitatively, consistent with the picture of dust particles trapped in a pressure bump, or large-scale vortex, in gas (Pinilla et al. 2012; Birnstiel et al. 2013; Lyra and Lin 2013). We also note that recent observations by ATCA at 34 GHz indicate that large grains are concentrated in the northern part of the disk (Casassus et al. 2015). Vortices should be confined within a narrow radial range of the scale comparable with the disk thickness in this case. It is hinted that there might exist small-scale structures close to the peak of dust distribution, as discussed at the end of section 5.6. Future higher resolution observations may reveal the small-scale structures within the bright dust ring. Recently, Mittal and Chiang

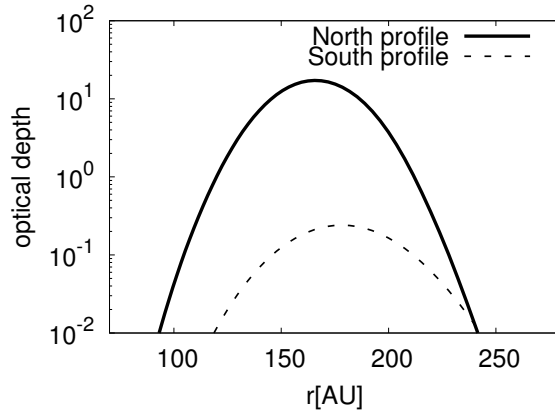


Fig. 27. Optical depth profiles for continuum emission. Solid line is for the north profile and the dashed line is for the south profile.

(2014) proposed that the global  $m = 1$  mode might play an important role in producing radially extended lopsided structures. One interesting prediction of this model is that dust grains with different sizes accumulate at different locations within the disk. This may be addressed by higher resolution observations in multi-wavelengths and modeling effort including several dust species. Another interesting mechanism for the formation of dust-rich regions is the secular gravitational instability (Ward 2000; Youdin 2011; Michikoshi et al. 2012; Takahashi and Inutsuka 2014). Takahashi and Inutsuka 2014 have done two-fluid analysis of gas and dust and shown that (multiple) ring-like structure with low gas-to-dust mass ratio can be created in self-gravitationally stable disks. Since initial gas mass should be relatively large in this case, significant gas dispersal should have occurred after the ring formation. This could be addressed, for example, by investigating the detailed kinematics of gas (e.g., Pontoppidan et al. (2011)).

## 6.2 Optical Depth and the Total Amount of Dust and Gas

### 6.2.1 Dust Optical Depth and Dust Properties

We have seen that the dust particles are strongly concentrated in the north region. The radial profiles of the optical depth at the observed frequency ( $\sim 340$  GHz) along the line of sight is shown in figure 27, and it is clear that, in the northern part, the optical depth of dust emission reaches  $\gtrsim 10$ .

We have used the dust model with the maximum size of 1 mm. This is purely an assumption of this study, in order to estimate the minimum amount of dust grains needed to explain the bright thermal emission by using the dust model having the maximum (or at least large within the models that are considered to be reasonable) opacity at sub-mm wavelengths. In the case of dust model with  $a_{\max} = 1$  mm, the dust continuum emission is dominated by scattered light component if the disk is optically thick, which is the case for the northern part, because the dust scattering coefficient is much greater than the absorption coefficient (figure 6). Figure 28 compares the radial profiles of dust continuum emission between calculations with and without scattered light component. We have artificially set the radiation energy density  $J_{\nu} = 0$  in equation (4) in the calculations to omit the scattered light component. In the northern part of the disk, the contribution from the scattered light component is a factor of  $\sim 5$  larger than that from the thermal emission that has not experienced scattering. In the southern part, where the disk is optically thin, the contribution from the scattered light component is much smaller.

There may be a variety of dust models that are able to reproduce observations. For example, the SED of HD 142527 can be reproduced by using irregularly-shaped micron-sized dust particles (Verhoeff et al. 2011). We have checked that the slope of SED in sub-mm range is consistent with observations in our model. Therefore, it is difficult to discriminate the dust size contributing most to sub-mm emission from current observations thus far. The scattering coefficient  $\kappa_s$  of micron-sized dust particles at sub-mm range is expected to be much smaller than that used in our work. If the scattered light component can be observed exclusively, it is possible to discriminate the dust size. The polarization of dust continuum emission, for example, can be a good tracer of the dust size (Kataoka et al. 2015).

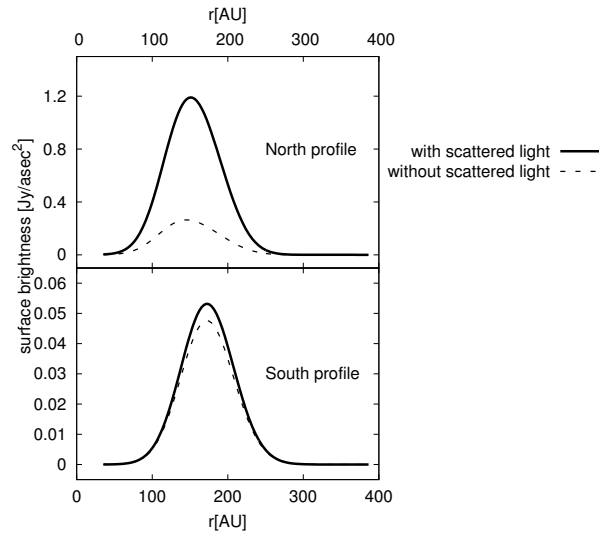


**Fig. 28.** Radial profiles of continuum emission calculated with (solid lines) and without (dashed lines) dust scattering. The left panel is for the north profile and the right panel is for the south profile.

### 6.2.2 Gas Optical Depth

We have used  $^{13}\text{CO } J = 3 - 2$  and  $\text{C}^{18}\text{O } J = 3 - 2$  emission to determine the gas structure. Figure 29 shows the radial profiles of the maximum optical depth of these lines (gas+dust optical depth, see also figure 30) for the reference disk models. It is shown that the gas is optically thick at the peak of the lines. The maximum optical depth reaches an order of unity even for the south model of  $\text{C}^{18}\text{O}$ .

Despite the fact that the lines are mostly optically thick, we have seen that the integrated intensity of gas emission becomes brighter as we increase the gas surface density (figures 11 and 12). This is because gas emission is not entirely optically thick for all the velocity channels. When the amount of gas is increased, gas emissivity is increased and therefore, there are more velocity channels that contribute to the gas brightness at each given spatial location. Figure 30 shows the radial profiles of the optical depth of the line wings. We show the optical depth at the velocity channels that are different from those giving the maximum optical depth (line center) by 0.12 km/s, 0.24 km/s, and 0.36 km/s. For all of the calculations shown in figure 30, the optical depth of the continuum emission (which is derived using the first term of equation (10)) is subtracted from gas+dust optical depth (which is derived using all the terms using the right hand side of (10)) to show the gas-only optical depth<sup>5</sup>. The line emission becomes optically thin at 0.2 – 0.3 km/s away from the line center. Since the values of moment 2 shown in figure 23 and 24 are  $\sim 0.3$  km/s at  $r \sim 150$  AU, we consider that the line emission is optically thin when the velocity deviates from the line center by (only) half width of the line, which is close to the value of moment 2. Therefore, line wings can be used to trace the gas surface density even in the case that the emission at line center is optically thick. We therefore consider that we can reasonably constrain the amount of gas even when it is optically thick. However, we yet see that  $^{13}\text{CO}$  is more insensitive to the change of the amount of gas compared to  $\text{C}^{18}\text{O}$ , which is more optically thin. Overall, we expect that the amount of gas has an uncertainty of a factor of  $\sim 2 - 3$ . For example, figure 11 indicates the models with  $\Sigma_0 = 2.325 \text{ g cm}^{-2}$  and  $\Sigma_0 = 0.845 \text{ g cm}^{-2}$  both explain the radial profiles of moment 0 in the north direction at  $r = 150 - 200$  AU region reasonably well. To better constrain the amount of gas, we may need observations of lines with lower optical depth by, for example, using rarer isotopologues or using lower transition lines. The values of isotope ratio and the dust opacity are also important in accurately determining the amount of gas. Since there is fair amount of dust, the line emission is affected by the dust absorption, especially in the northern part of the disk. The scattering of gas lines by dust particles, which is not included in our model, can also be effective in determining the observed spatio-kinematic patterns.

### 6.2.3 Total Amount of Gas and Dust

We now discuss the total amount of dust and gas indicated from our modeling. We have two surface density distribution models, namely the north and south model, for each dust and gas.

For dust mass, we obtain  $M_{\text{dust}} = 3.5 \times 10^{-3} M_{\odot}$  for the north profile and  $M_{\text{dust}} = 7 \times 10^{-5} M_{\odot}$  for the south profile when

<sup>5</sup> In other words, gas-only optical depth is calculated by taking into account only the second term of the right hand side of equation (10)

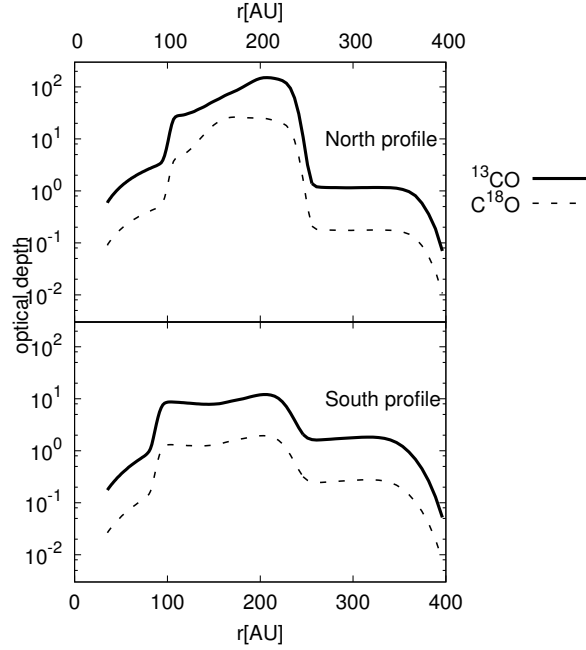


**Fig. 29.** The line-of-sight optical depth of  $^{13}\text{CO}$  (solid line) and  $\text{C}^{18}\text{O}$  (dashed line). Top panel shows the optical depth of the northern part of the disk and the bottom panel shows that of the southern part.

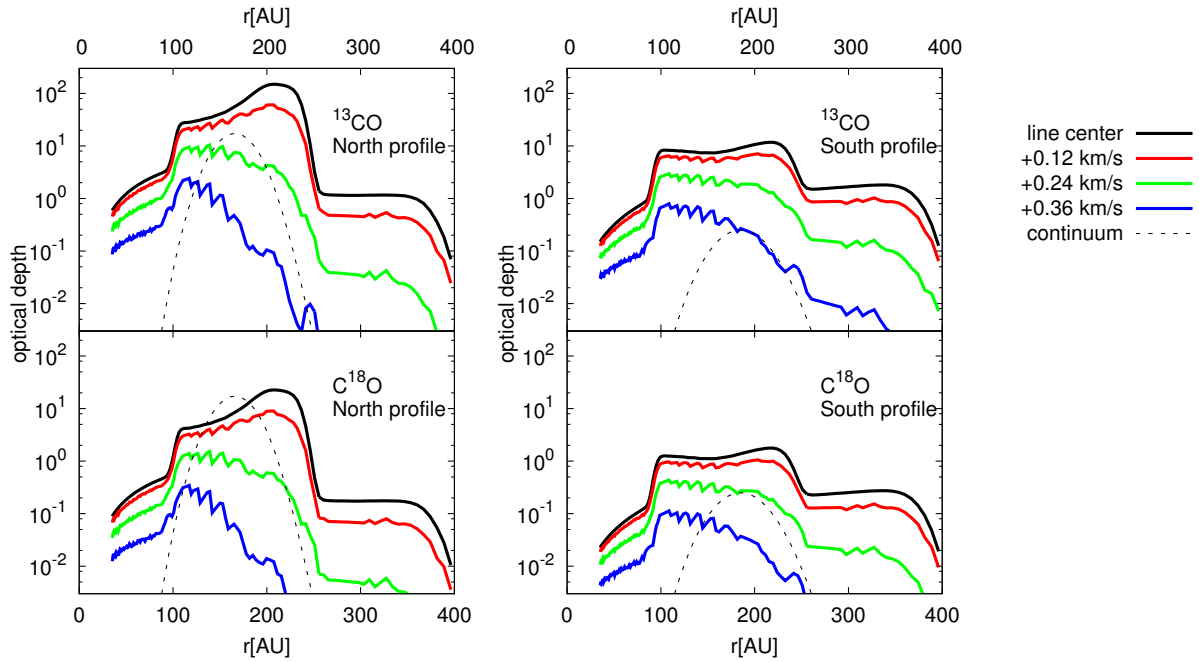


**Fig. 30.** The line-of-sight optical depth of the north profile (left) and south profile (right). The upper panels show the optical depth of  $^{13}\text{CO}$  and the lower panels show that of  $\text{C}^{18}\text{O}$ . In each panel, the line-of-sight optical depth of the line center (the maximum optical depth of all the channels) is shown by black solid lines and that of the channels offset from the line center by 0.12 km/s, 0.24 km/s, 0.36 km/s is shown in red, green, and blue lines respectively. The optical depth of the continuum emission (black dashed lines) is subtracted for all of the gas optical depth.



integrated over the entire disk. Verhoeff et al. (2011) obtained the dust mass of  $1 \times 10^{-3} M_{\odot}$  from their SED modeling. Considering that the bright arc of dust emission extends about  $\sim 1/3$  of the whole azimuth, the value of dust mass we have obtained is similar to their results, despite the difference of grain properties. For gas mass, we obtain  $M_{\text{gas}} = 1.8 \times 10^{-2} M_{\odot}$  and  $M_{\text{gas}} = 5.7 \times 10^{-3} M_{\odot}$  for the reference north and south models, respectively, when integrated over the disk within 400 AU.<sup>6</sup>

Although the total gas mass could have a factor of  $\sim 2 - 3$  uncertainty as noted before, the overall gas-to-dust mass ratio may be  $\lesssim 10 - 30$ , which is smaller than the interstellar value of 100. The derived gas-to-dust mass ratio is likely to be an upper limit. Since the north region is optically thick, the dust emission is not very sensitive to the increase in the amount of dust (see appendix 2). We should also remember that the dust particles have relatively large opacity (and therefore emissivity) in sub-mm range ( $a_{\text{max}} = 1$  mm). If smaller grains are more abundant, we expect that the disk midplane, where dust emission originates, is colder while the disk surface, where optically thick gas emission originates, is warmer (Inoue et al. 2009). Consequently, even if small grains are more abundant, we expect brighter emission in gas while fainter in dust, resulting in smaller gas-to-dust ratio. We therefore propose that the dispersal of gas, or at least the depletion of CO gas, may have already taken place in the disk of HD 142527. However, it should be noted that detailed modeling with different dust grain properties is necessary to confirm this. Grain size and shape can strongly affect the observed emission properties (e.g., Min et al. 2003).

Perez et al. (2015) derived the total gas mass of  $0.1 M_{\odot}$  from their modeling effort. They used the model where the temperature is assumed to be 50 K at 50 AU with  $r^{-0.3}$  profile and the Doppler  $b$  parameter is assumed to be  $50 \text{ m s}^{-1}$ . Their radial temperature profile is flat and the temperature is smaller than our model by a factor of  $\sim 1.7$  at  $r = 100$  AU. We have calculated how the assumptions of the temperature and the line width affect the results by setting those parameters to be the same as Perez et al. (2015) but the density is given by our reference model (equation (16) and table 6). The values of  $^{13}\text{CO } J = 3 - 2$  moment 0 is smaller by a factor of  $\sim 2$  at  $r \sim 100$  AU with this model. The impact of line width on moment 0 profile comes from the fact that there are less velocity channels that contribute to integrated intensity at each spatial position (see also the discussion in section 6.2.2). To compensate this by varying the amount of gas (parameter  $\Sigma_0$  in our model), we need to increase the value of  $\Sigma_0$  by a factor of  $\sim 5 - 10$ , as seen in figure 11. Consequently, we consider that the difference of the total amount of gas comes from the different assumption of the temperature and the line width. The temperature profile used by Perez et al. (2015) comes from  $^{12}\text{CO } J = 2 - 1$  observations, which may be smoothed by the relatively large beam. High resolution gas observations will play a decisive role in determining the distribution and total mass of gas component more accurately.

### 6.3 Gas Bump Structures in Model

The north radial profiles of the moment 0 of the reference model is bumpy at  $r \sim 170 - 200$  AU, where dust emission is the brightest. As discussed in section 5.3, these bumps and troughs in gas emission arise because the continuum emission is very bright and comes from relatively narrow radial range. Since the line emission is partially hidden by dust, there is a significant effect on line emission when dust continuum is subtracted.

There are at least two possible ways to obtain smoother moment 0 profiles. One possibility is to increase the amount of gas at the location of the peak of dust emission locally. In other words, there may be more detailed, small-scale (several tens of AU scale) structures in the radial direction than we have considered. As seen in figure 11, a factor of  $\sim 3$  larger gas surface density locally at the peak of dust distribution may explain the observed values of moment 0 at this region. Since the dust emission is barely resolved in the radial direction, it may be difficult to see such small-scale variation of gas distribution. Higher angular resolution observations of gas is necessary to confirm this possibility.

The other possibility is to consider more optically thin dust particles. Since the dust scattering opacity is  $\sim 10$  times larger than the absorption opacity in our dust model, the total extinction coefficient of dust is dominated by the scattering opacity and is comparable with gas opacity (figure 30). Therefore, if the dust scattering coefficient is much smaller than considered in this paper, the gas emission can be brighter so the effects of continuum subtraction is more insignificant. Smaller dust particles may be one solution, but in this case, it is necessary to have larger amount of dust because the absorption coefficient (and therefore dust emissivity) is also small.

A large (effective) emissivity and small scattering coefficient may be obtained simultaneously if we consider dust sedimentation. In our framework, the gas-to-dust ratio is constant in the vertical direction so large ( $\sim \text{mm}$  in size) dust particles reside even in the upper layer of the disk. However, such large particles may be sedimented to the disk midplane. The surface of the CO emission resides in the upper layer of the disk, and therefore there may only be small dust particles having small scattering coefficient around

<sup>6</sup> Inside 400 AU, the gas mass is dominated by the gas residing within  $r \lesssim r_{\text{out}}$  although we have assumed that constant surface density in the radial direction for outer tenuous gas.

the gas surface. The gas emission is not hidden by dust very much in this case and therefore the effects of the subtraction of the continuum emission is less significant. More sophisticated models that take into account the dust particle motion is necessary to verify this possibility. Also, the optical properties of the dust particles and its impact on observations should be carefully investigated. Detailed modeling in tandem with scattered light observations in near infrared (NIR; see also section 6.5), which is sensitive to the small dust particles in the upper layer of the disk, may be a key to verify this possibility.

#### 6.4 Discrepancy of Moment 1 at Inner Radii

In the moment 1 profiles of the south gas models, we see that the reference model shows slower speed than observed at  $r < 100$  AU for  $^{13}\text{CO}$  but faster at  $r < 50$  AU for  $\text{C}^{18}\text{O}$ , as shown in figure 24. We have checked that this discrepancy is also present when the surface density profiles for the remaining gas inside the cavity is taken to be constant so the details of the radial profile of gas surface density do not alter the results.  $\text{C}^{18}\text{O}$  data may be affected by the lower signal-to-noise ratio at high velocity channels, but the detection of  $^{13}\text{CO}$  at  $r \sim 50 - 100$  AU region is robust.

It is natural that the observed velocity should become smaller than Keplerian as one goes to inner radii, where the disk is barely spatially resolved in channel maps and the signal is weak. The gradient of line-of-sight velocity within the beam is large at inner radii and therefore emission at many velocity channels are averaged. Weak high velocity component may be discarded when the sensitivity is limited. These effects should properly be incorporated in our modeling since we convolve each channel map image by the Gaussian beam before calculating the model moment maps (see section 3.2). Therefore, the discrepancy between the observations and models might indicate that, in the southern region, the gas velocity is significantly faster than Kepler velocity at least for  $^{13}\text{CO}$  at inner radii. Rosenfeld et al. (2014) discussed that there may be a fast radial flow in the inner region of the disk of HD 142527 based on  $^{12}\text{CO}$  and  $\text{HCO}^+$  data taken by ALMA Cycle 0. Marino et al. (2015) suggested that the inner disk is significantly inclined relative to the outer disk based on the modeling of scattered light in the H-band. The discrepancy between the reference model and observations of  $^{13}\text{CO}$  for the southern region may also indicate the existence of such dramatic change of the inner disk structure. Observations with better spatial resolution are essential to clarify this point.

#### 6.5 Outer Tenuous Gas and Scattered Light in Near Infrared

We have seen that there should be some amount of tenuous gas at  $r > 250$  AU. The surface density of the tenuous gas is estimated to be  $\sim 7 \times 10^{-3} - 2 \times 10^{-2}$  g/cm<sup>2</sup>. It is known that the HD 142527 disk shows an extended ( $\sim 300$  AU scale) scattered light emission in NIR observations (Fukagawa et al. 2006; Casassus et al. 2012; Canovas et al. 2013; Rodigas et al. 2014). Especially, the large-scale spiral structure appears from the south of the disk and extends towards the west.

The extended scattered light emission in NIR may be connected to the existence of tenuous gas at outer radii. In NIR direct imaging observations, scattered light by small (typically,  $\sim 1 \mu\text{m}$  in size) dust grains at the disk surface is observed. Since such particles are well coupled with gas, we expect that small grains are distributed as gas is. The amount of tenuous gas ( $\sim 0.02$  g cm<sup>-2</sup> at  $r \sim 300$  AU in the south model) is probably enough to make the disk optically thick in NIR range, where dust opacity may be several tens of cm<sup>2</sup> per unit gram of gas in the case of  $a_{\text{max}} \sim 1 \mu\text{m}$  if gas-to-dust ratio is 100 in the outer  $r > 250$  AU region (e.g., D'Alessio, Calvet and Hartmann 2001; Aikawa and Nomura 2006). Considering the detection limit of dust continuum, we expect that such (small) grains contained in the outer tenuous gas component are neither observable nor massive enough to contribute to the gas-to-dust ratio within 400 AU (see section 6.2.3). To further investigate the distribution of small grains, we need simultaneous modeling of scattered light and mm-emission, which is beyond the scope of this paper.

### 7 Conclusion

We have presented the models for gas and dust distribution for the disk around HD 142527 by using a series of axisymmetric models and by comparing the radial profiles of dust and gas emission. The schematic picture of the gas and dust distribution is shown in figure 31. Below, we list the main conclusions of our work.

1. The dust particles are confined in a ring whose surface density profile is described by a Gaussian function in the radial directions with the width of  $w_d \sim 30$  AU for both the north and south regions. The location of the ring is slightly different between the north ( $r_d \sim 170$  AU) and south profiles ( $r_d \sim 200$  AU). To account for the strong azimuthal asymmetry of the continuum emission, the surface density of the dust ring is different by a factor of  $\sim 70$  between the northern and southern part of the ring. Note that these results are based on the dust model with the maximum size of 1 mm, where the opacity at sub-mm wavelengths is large and

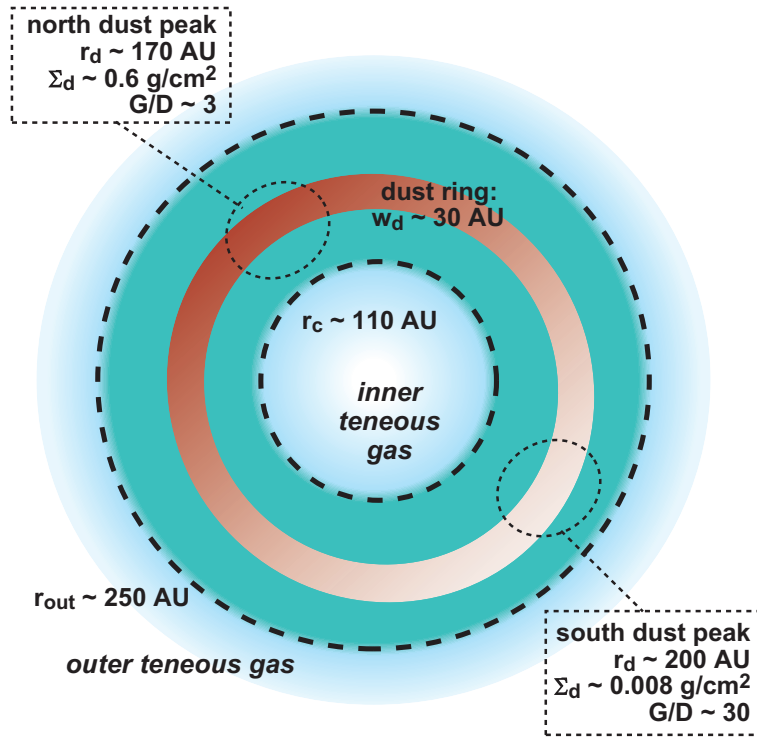


**Fig. 31.** Schematic picture of the disk around HD 142527. Green colors indicate gas distribution and brown indicate dust distribution. The dust ring with the width of  $w_d \sim 30$  AU is located at  $r \sim 170 - 200$  AU. The ring surface density is differ by a factor of  $\sim 70$  in the northern and the southern part. The gas surface density is more radially extended. The gas distribution shows a bump-like structure from  $\sim 100$  AU to  $\sim 250$  AU but there is remaining, tenuous gas component both inner and outer radii.

therefore, we expect that the dust mass derived in our work is close to the lower limit.

2. The gas distribution is azimuthally more symmetric than dust distribution. The amount of gas in the northern region is indicated to be  $\sim 3$  times as large as that in the southern region.
3. The gas radial surface density distribution is more radially extended than dust. The radial profiles of the moment maps of  $^{13}\text{CO } J = 3 - 2$  and  $\text{C}^{18}\text{O } J = 3 - 2$  emission can be described with the power-law profile between  $\sim 100$  AU and  $\sim 250$  AU, along with the remaining gas inside the cavity and with tenuous outer gas at  $r > 250$  AU. Small-scale ( $\sim 50$  AU-scale) variation in the radial directions of gas distribution with a factor of  $\sim 3$  is also indicated around the peak of dust distribution.
4. Gas-to-dust ratio varies significantly within the disk. At the peak of the dust distribution, it is  $\sim 3$  in the northern part of the disk while  $\sim 30$  in the south. The gas-to-dust ratio over the whole disk is expected to be  $\sim 10 - 30$  within 400 AU, indicating that gas depletion has already occurred in this system.

We have used a series of axisymmetric disk models to do systematic parameter search while keeping the problem tractable. Since the CO isotopes used in this observation have turned out to be optically thick, observations of rarer isotopes or lower transitions are necessary to better constrain the amount of gas. More elaborate dust models will also be required to fully constrain the disk parameters and to account for observations at other wavelengths.

We thank Sebastian Perez for useful discussions. We also thank an anonymous referee for careful reading and useful suggestions to improve the paper. This paper makes use of the following ALMA data: ADS/JAO.ALMA#2011.0.00318.S. ALMA is a partnership of ESO (representing its member states), NSF (USA), and NINS (Japan), together with NRC (Canada) and NSC and ASIAA (Taiwan), in cooperation with the Republic of Chile. The Joint ALMA Observatory is operated by ESO, AUI/NRAO and NAOJ. This work is partially supported by JSPS KAKENHI Grant Numbers 23103004, 26800106 and 26400224.

## Appendix 1 Details on $^{13}\text{CO}$ and $\text{C}^{18}\text{O}$ results

Figures 32, 33 and 34 show the channel maps of  $^{13}\text{CO}$  from which the moment maps shown in figure 3 are created. Figures 35 and 36 show the channel maps of  $\text{C}^{18}\text{O}$  from which the moment maps shown in figure 4 are created.

As described in section 2.3, a constant (systemic) velocity of  $3.7 \text{ km s}^{-1}$  is found along  $PA = 71^\circ \pm 2^\circ$ , which can be regarded as the direction of the minor axis of the system. The position-velocity (P-V) diagram along the major axis ( $PA = -19^\circ$ ; figure 37) was fitted by circular Keplerian motion for the emission detected above  $5\sigma$  (figure 37). The systemic velocity, position of the center of mass (the central star), and inclination relative to an observer are set as free parameters, whereas the central stellar mass is fixed in the range of  $2.2 \pm 0.3 M_\odot$  (Verhoeff et al., 2011). The best-fitted parameters obtained by  $\chi^2$ -minimization are in good agreement between  $^{13}\text{CO}$  and  $\text{C}^{18}\text{O}$ . Using  $^{13}\text{CO}$  detected with a higher S/N, the system inclination angle is estimated as  $i = 26.5^{+2.2}_{-1.7}$  degrees, where the uncertainty arises from the error in the stellar mass. Note that  $i$  is not large enough to yield reasonable constraints on both the stellar mass and the inclination (Simon et al. 2000). The systemic velocity is estimated to be  $3.72 \pm 0.02 \text{ km s}^{-1}$  in  $v_{\text{LSR}}$ , and the obtained location of the center of mass matches that of the compact component of the continuum emission, which most likely represents the inner disk. Figure 37 also shows the curves for the Keplerian rotation with the parameters adopted in the modeling, i.e.,  $i = 27^\circ$ ,  $M = 2.2 M_\odot$  and the systemic velocity of  $3.7 \text{ km s}^{-1}$  in  $v_{\text{LSR}}$ . No significant deviation from the Keplerian motion was detected within the effective resolution of  $0.2 \text{ km s}^{-1}$  in our observations.

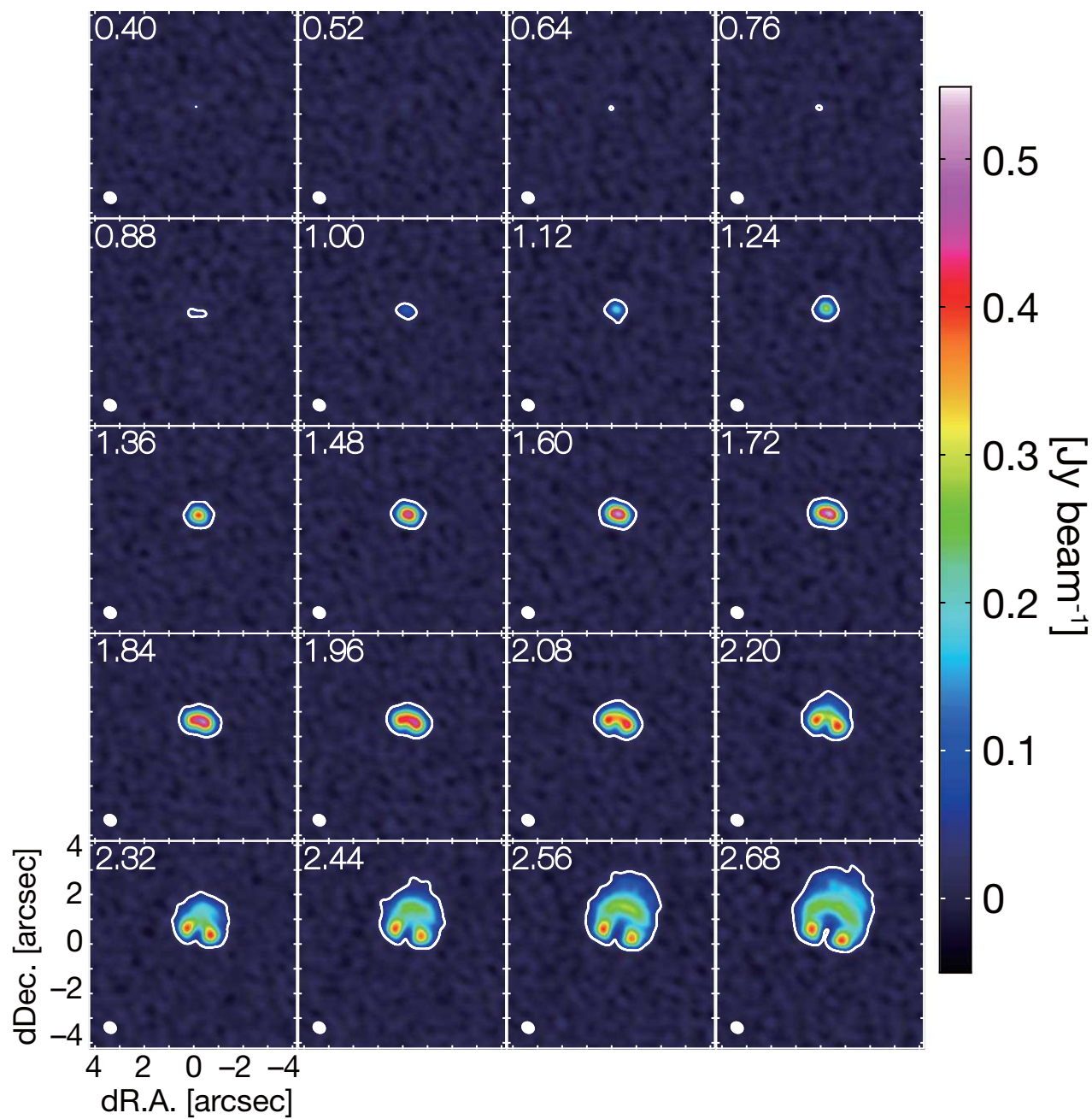


Fig. 32. Channel maps of  $^{13}\text{CO}$  ( $J = 3 - 2$ ). The LSR velocity is shown in the top left corner of each panel, and the synthesized beam,  $0''.50 \times 0''.42$  with the major axis  $PA = 57.4^\circ$ , is indicated by the ellipse in the bottom left corner of each panel. The white contours are the  $5\sigma$  level, or  $32 \text{ mJy beam}^{-1}$ .



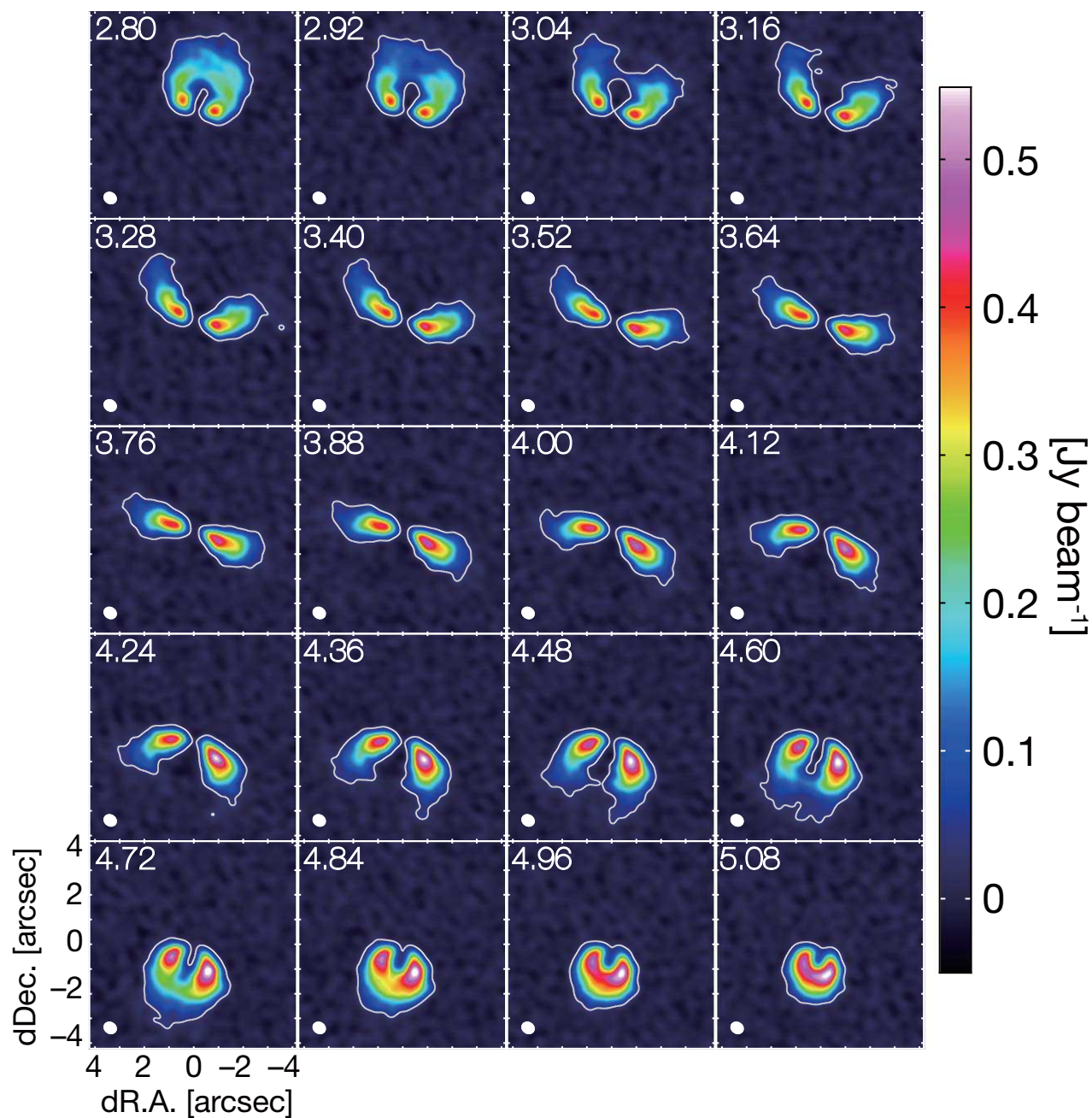


Fig. 33. Channel maps of  $^{13}\text{CO}$  ( $J = 3 - 2$ ), continued from figure 32.



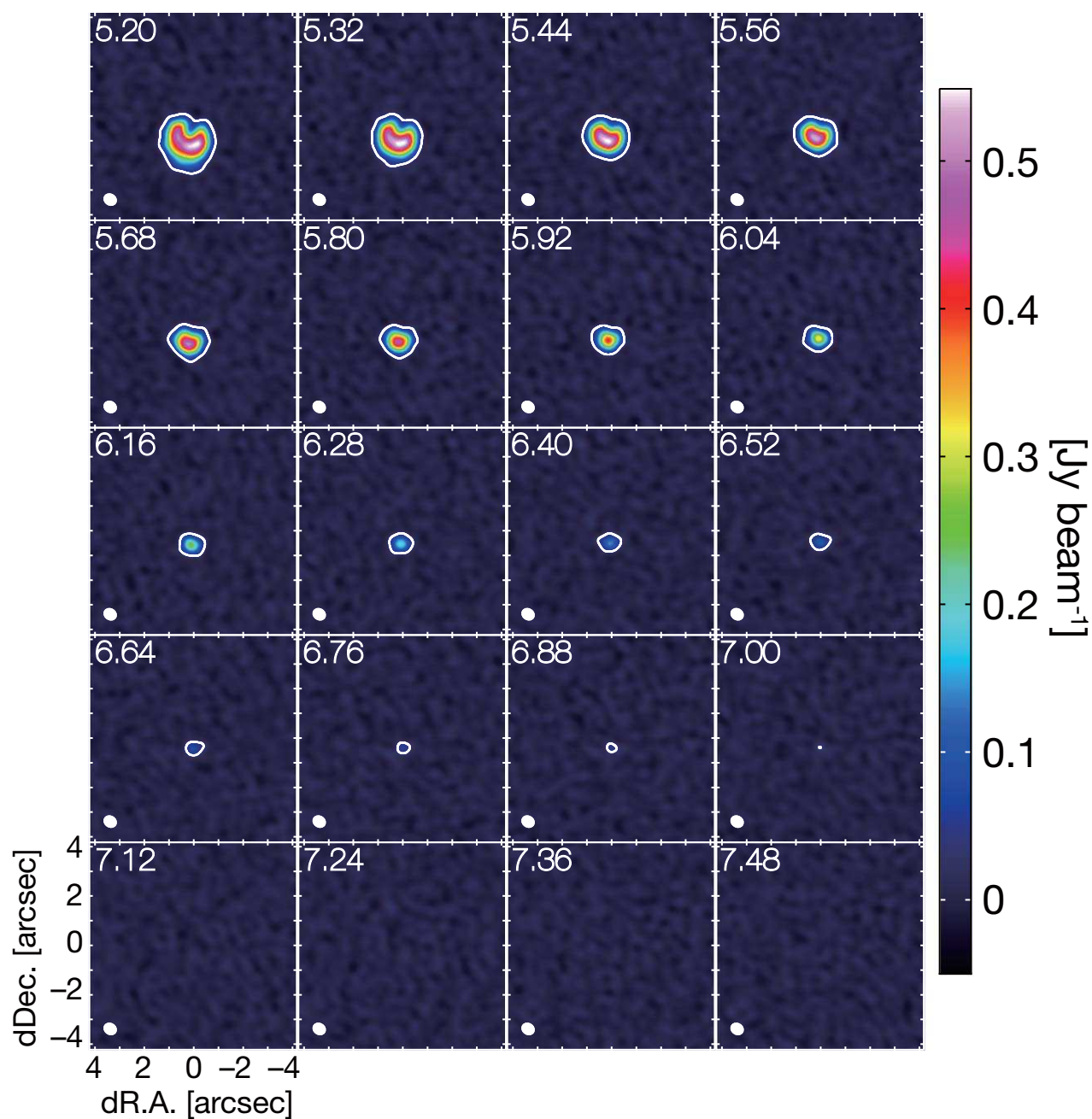
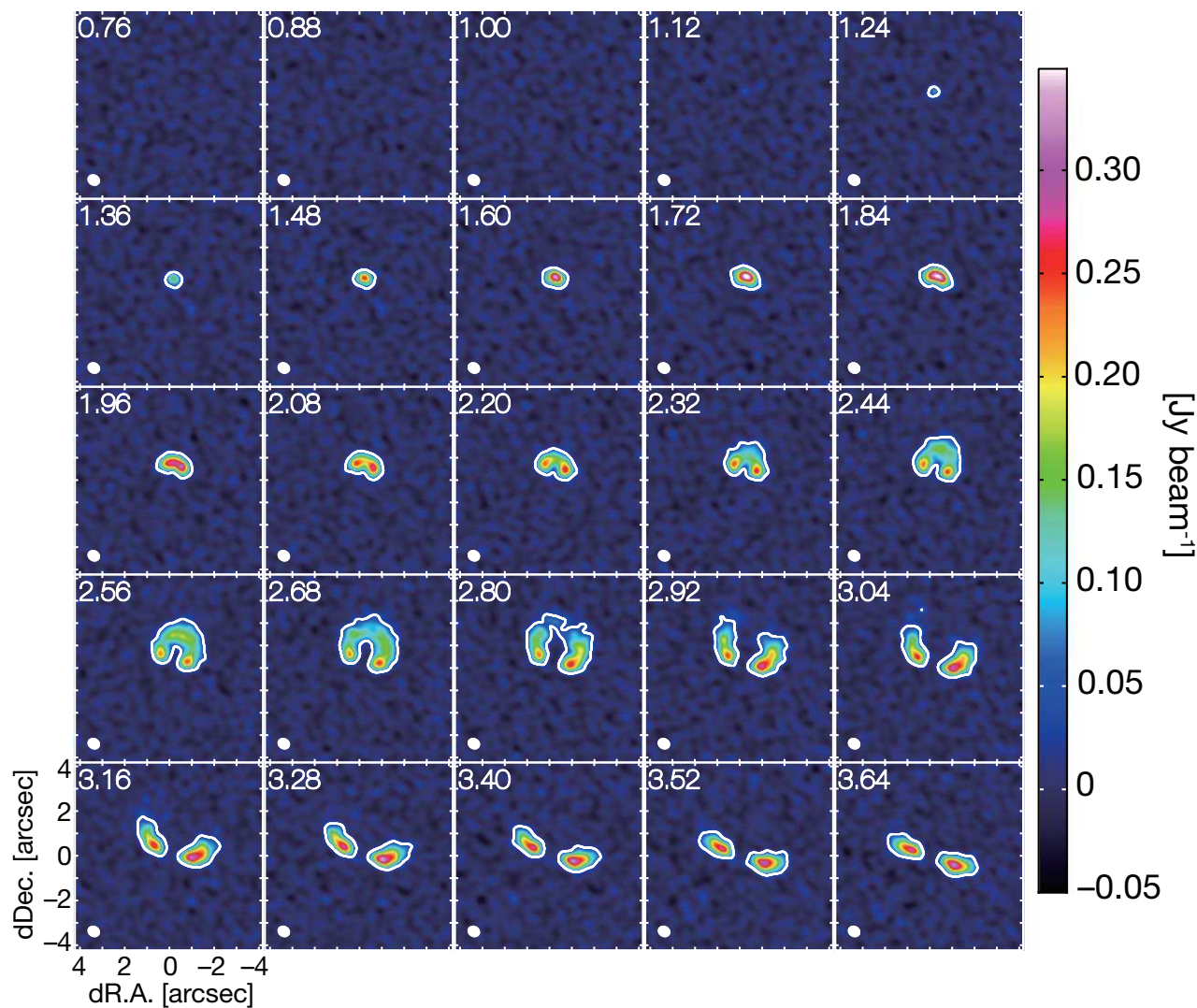


Fig. 34. Channel maps of  $^{13}\text{CO}$  ( $J = 3 - 2$ ), continued from figure 33.



**Fig. 35.** Channel maps of  $\text{C}^{18}\text{O}$  ( $J = 3 - 2$ ). The LSR velocity is shown in the top left corner of each panel, and the synthesized beam,  $0''.50 \times 0''.42$  with the major axis  $PA = 60.6^\circ$ , is indicated by the ellipse in the bottom left corner of each panel. The white contours are the  $5\sigma$  level, or  $41.5 \text{ mJy beam}^{-1}$ .

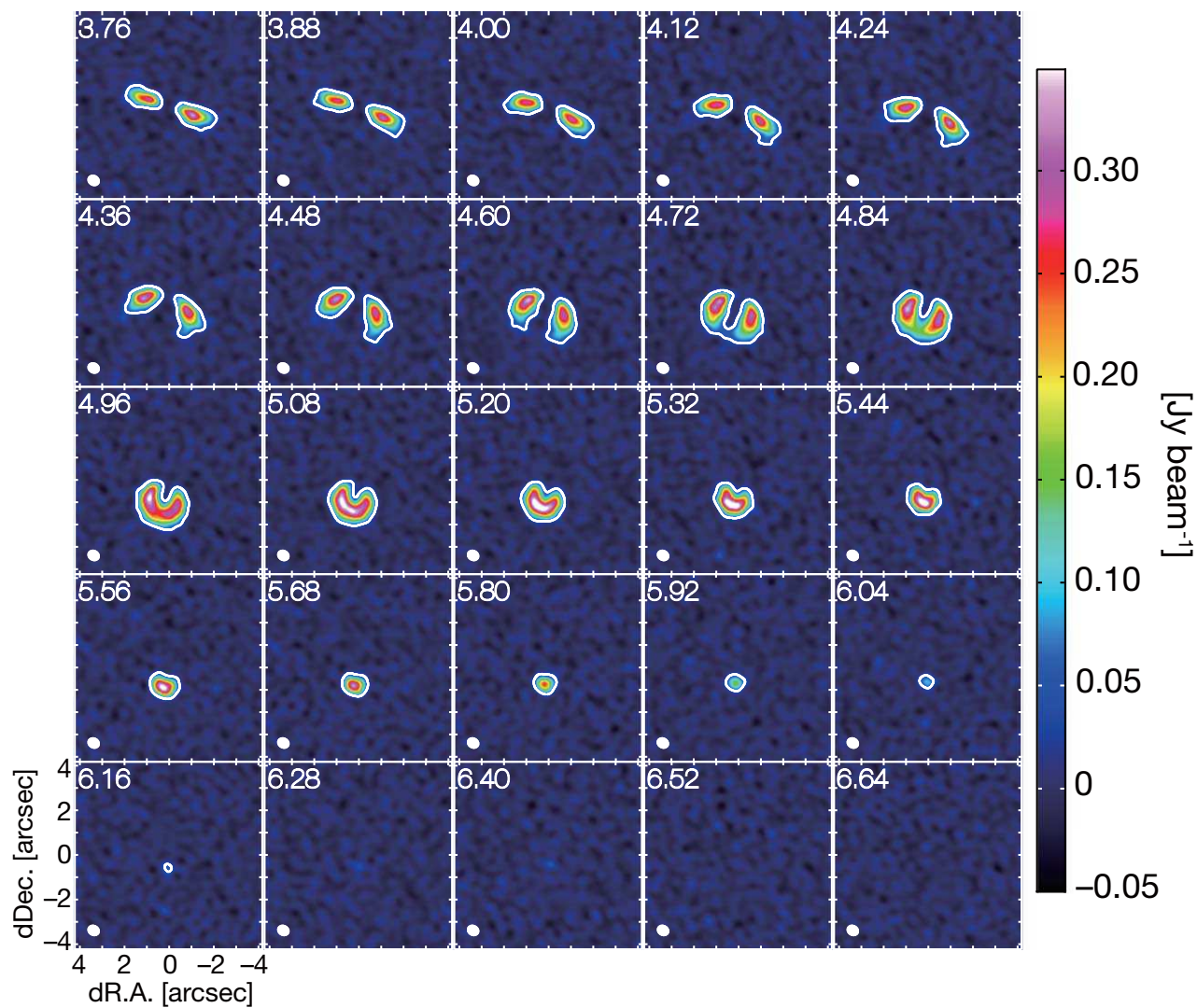


Fig. 36. Channel maps of  $\text{C}^{18}\text{O}$  ( $J = 3 - 2$ ), continued from figure 35.

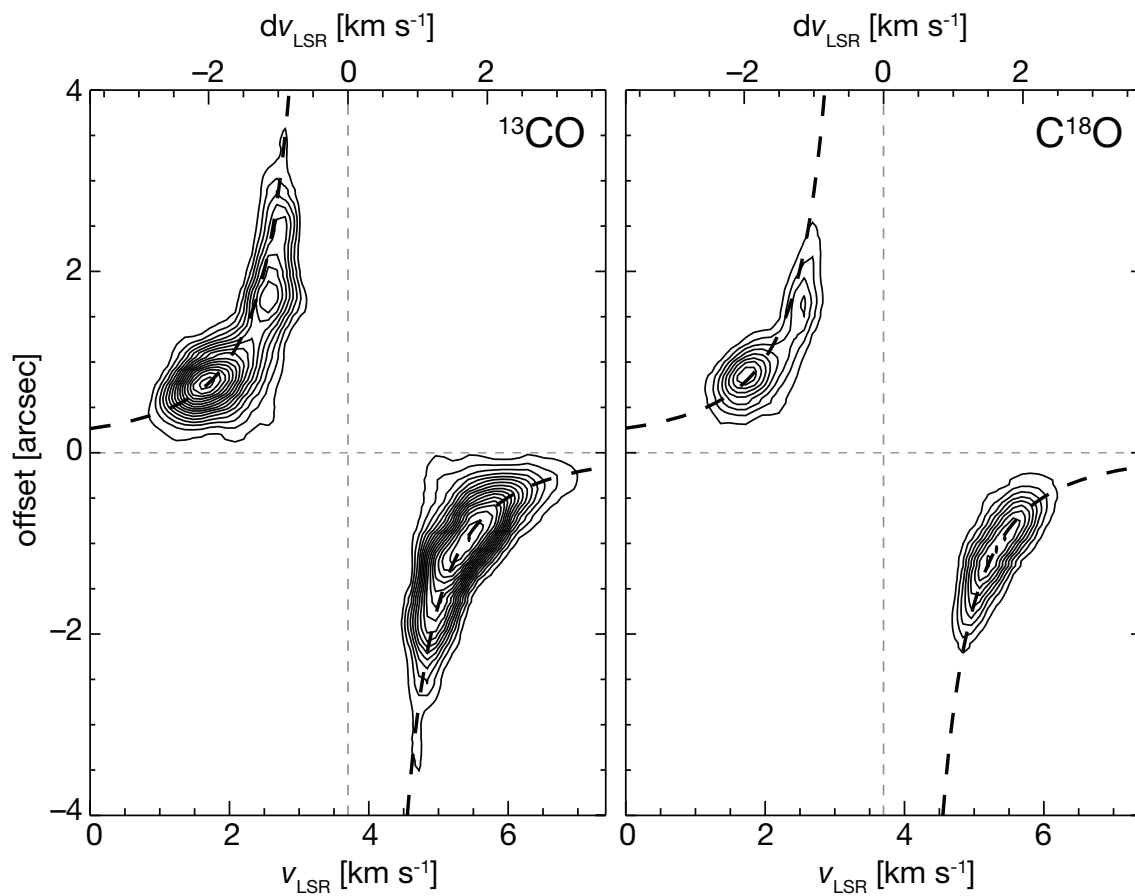


Fig. 37. The PV diagrams along the major axis ( $PA = 341^\circ$ ) in  $^{13}\text{CO}$  and  $\text{C}^{18}\text{O}$  ( $J = 3 - 2$ ) lines. The contour spacing is  $5\sigma$ , starting at the  $5\sigma$  level. The dashed curves in each panel indicate the Keplerian rotation when  $M = 2.2M_\odot$  and the inclination angle  $i = 27^\circ$ .



## Appendix 2 Details of parameter search for dust distribution

In this section, we present the results of parameter search for dust distribution models. We vary the parameters for dust distribution  $\Sigma_{d,0}$ ,  $r_d$  and  $w_d$  and look for a set of parameters that best reproduces the dust continuum observations. Here, we exclusively show the results of the north region where dust emission is optically thick. For the south region, the disk is optically thin and the parameter search is straightforward.

For each set of the parameters  $(\Sigma_{d,0}, r_d, w_d)$ , we calculate the dust continuum emission and the model images. The model images are convolved with the Gaussian beam with the size of the observations. The convolved radial profiles of the surface brightness is fitted by the Gaussian function given in equation (1). The derived parameters  $(I_p, r_0, w)$  are compared with those derived from observations  $(I_{p,obs}, r_{0,obs}, w_{obs})$ . Tables 7, 8, and 9 show the results when  $\Sigma_{d,0}$ ,  $r_d$ , and  $w_d$  are varied, respectively.

The peak brightness of dust emission depends weakly on the assumed peak surface density. It is 1.17 and 1.25 Jy/asec<sup>2</sup> for  $\Sigma_{d,0} = 0.5$  and 0.7 g/cm<sup>2</sup>, respectively, when other parameters are fixed at  $r_d = 173$  AU and  $w_d = 27$  AU (the best-fit parameters; table 7). In other words, a factor of 1.4 increase in surface density results in only  $\sim 7\%$  in the surface brightness. The peak brightness depends weakly on  $r_d$  and  $w_d$  as well. It is 1.24 and 1.19 Jy/asec<sup>2</sup> for  $r_d = 163$  and 183 AU, respectively (table 8), meaning that 12 % change in  $r_d$  results in 4 % change in the peak brightness. In this case,  $r_0$  also changes by  $\sim 20$  AU so  $r_0$  is more affected by the change in  $r_d$ . When  $w_d$  is varied from 22 to 34 AU, the peak brightness changes from 1.12 to 1.28 Jy/asec<sup>2</sup> (table 9), meaning that  $\sim 50\%$  change in the width of dust distribution results in  $\sim 14\%$  change in the peak brightness. In this case, the width of surface brightness changes by  $\sim 20\%$  so it is more affected than the peak brightness.

Model Parameters ( $\Sigma_{d,0}$ [g/cm <sup>2</sup> ], $r_d$ [AU], $w_d$ [AU])	Model Results ( $I_p$ [Jy/asec <sup>2</sup> ], $r_0$ [AU], $w$ [AU])
(0.5, 173, 27)	(1.17, 152, 50)
(0.6, 173, 27)	(1.20, 153, 50)
(0.7, 173, 27)	(1.25, 150, 50)

**Table 7.** Results of model dust continuum emission of the north profile with different  $\Sigma_{d,0}$ . The observed parameters are ( $I_{p,obs}, r_{0,obs}$  [AU],  $w_{obs}$  [AU]) = (1.2 Jy/asec<sup>2</sup>, 152 AU, 51 AU).

Model Parameters ( $\Sigma_{d,0}$ [g/cm <sup>2</sup> ], $r_d$ [AU], $w_d$ [AU])	Model Results ( $I_p$ [Jy/asec <sup>2</sup> ], $r_0$ [AU], $w$ [AU])
(0.6, 163, 27)	(1.24, 141, 51)
(0.6, 173, 27)	(1.20, 153, 50)
(0.6, 183, 27)	(1.19, 161, 51)

**Table 8.** Results of model dust continuum emission of the north profile with different  $r_d$ . The observed parameters are ( $I_{p,obs}, r_{0,obs}$  [AU],  $w_{obs}$  [AU]) = (1.2 Jy/asec<sup>2</sup>, 152 AU, 51 AU).

Model Parameters ( $\Sigma_{d,0}$ [g/cm <sup>2</sup> ], $r_d$ [AU], $w_d$ [AU])	Model Results ( $I_p$ [Jy/asec <sup>2</sup> ], $r_0$ [AU], $w$ [AU])
(0.6, 173, 22)	(1.12, 154, 47)
(0.6, 173, 27)	(1.20, 153, 50)
(0.6, 173, 34)	(1.28, 146, 56)

**Table 9.** Results of model dust continuum emission of the north profile with different  $w_d$ . The observed parameters are ( $I_{p,obs}, r_{0,obs}$  [AU],  $w_{obs}$  [AU]) = (1.2 Jy/asec<sup>2</sup>, 152 AU, 51 AU).

## References

- Aikawa, Y., Nomura, M., 2006, ApJ, 642, 1152
- Anders, E., Grevesse, N., 1989, *Geochemica et Cosmochimica Acta*, 53, 197
- D'Alessio, P., Calvet, N., & Hartmann, L. 2001, ApJ, 553, 321
- Andrews, S. M., Wilner, D. J., Espaillat, C., et al. 2011, ApJ, 732, 42
- Mihalas, D., Mihalas, B. W. 1984, *Foundations of Radiation Hydrodynamics*, New York, Oxford University Press
- Beckwith, S. V. W., Sargent, A. I., Chini, R. S., & Guesten, R. 1990, AJ, 99, 924
- Biller, B., Lacour, S., Juhász, A. 2012, ApJ, 753, id.L38
- Birnstiel, T., Dullemond, C. P., Pinilla, P. 2013, A&A, 550, id.L8
- Bruderer, S., van der Marel, N., van Dishoeck, E. F., van Kempen, T. A. 2014, A&A, 562, id.A26
- Calvet, N., D'Alessio, P., Hartmann, L., et al. 2002, ApJ, 568, 1008
- Canovas, H., Ménard, F., Hales, A., Jordán, A., Schreiber, M. R., Casassus, S., Gledhill, T. M., Pinte, C., 2013, A&A, 556, A123
- Casassus, S., Perez, M., S., Jordán, A., Ménard, F., Cuadre, J., Schreiber, M. R., Hales, A. S., Ercolano, B. 2012, ApJ, 754, id.L31
- Casassus, S., van der Plas, G., Perez, S. M., et al. 2013, *Nature*, 493, 191
- Casassus, S., Wright, C., Marino, S. et al., 2015, ApJsubmitted, arXiv:1505.07732
- Dubulle, B., Morfill, G., Sterzik, M. 1995, *Icarus*, 114, 237
- Fujiwara, H., Honda, M., Kataza, H., et al. 2006, ApJ, 644, L133
- Fukagawa, M., Tamura, M., Itoh, Y., Kudo, T., Imaeda, Y., Oasa, Y., Hayashi, S. S., Hayashi, M. 2006, ApJ, 636, L153
- González, M., Audit, E., Huynh, P., 2007, A&A, 464, 429
- Fukagawa, M., Tsukagoshi, T., Momose, M. et al., 2013, PASJ, 65, No.L14
- Inoue, A. K., Oka, A., Nakamoto, T., 2009, MNRAS, 393, 1377
- Kataoka, A., Muto, T., Momose, M., Tsukagoshi, T., Fukagawa, M., Shibai, H., Hanawa, T., Murakawa, K., 2015, ApJaccepted, arXiv:1504.04812
- Kanno, Y., Harada, T., Hanawa, T. 2013, PASJ, 65, No.72
- Lyra, W., Lin, M.-K., 2013, ApJ, 775, id.17
- Min, M., Hovenier, J.-W., de Koter, A., 2003, A&A, 404, 35
- Mendigutía, I., Fairlamb, J., Montesinos, B., Oudmeijer, R. D., Najita, J. R., Brittain, S. D., van den Ancker, M. E., 2014, ApJ, 790, id.21
- Kamp, I., Dullemond, C. P., 2004, ApJ, 615, 991
- Marino, S., Perez, S., Casassus, S. 2015, ApJL, 798, id.L44
- Michikoshi, S., Kokubo, E., and Inutsuka, S., 2012, ApJ, 746, id.35
- Mittal, T. and Chiang, E., 2014, 2015, ApJL, id.L25
- Nomura, M., Millar, T. J., 2005, A&A, 438, 923
- Perez, S., Casassus, S., Ménard, F., et al. 2015, ApJ, 798, id.85
- Pinilla, P., Birnstiel, T., Ricci, L., Dullemond, C. P., Uribe, A. L., Natta, A. 2012, A&A, 538, id.A114
- van der Plas, G., Casassus, S., Ménard, F., et al. 2014, ApJ, 792, L25
- Pavlyuchenkov, Y., Semenov, D., Henning, T., Guilloteau, S., Piétu, V., Launhardt, R., Dutrey, A. 2007, ApJ, 669, 1262
- Pontoppidan, L. M., Blake, G. A., Smette, A., 2011, ApJ, 733, 84
- Qi, C., D'Alessio, P., Öberg, K. I., et al. 2011, ApJ, 740, 84
- Rameau, J., Chauvin, G., Lagrange, A.-M., et al. 2012, A&A, 546, A24
- Rodigas, T. J., Follette, K. B., Weinberger, A., Close, L., Hines, D. C., 2014, ApJ, 791, id.L37
- Rosenfeld, K., Chiang, E., Andrews, S. M., 2014, ApJ, 782, id.9
- Simon, M., Dutrey, A., & Guilloteau, S. 2000, ApJ, 545, 1034
- Strom, K. M., Strom, S. E., Edwards, S., Cabrit, S., Strutskie, M. F. 1999, AJ, 97, 1451
- Takahashi, S. Z., Inutsuka, S. 2014, ApJ, 794, 55
- Verhoeff, A. P., Min, M., Pantin, E., et al. 2011, A&A, 528, id.A91
- Waelkins, C., Waters, L. B. F. M., de Graauw, M. S., 1996, A&A, 315, L245
- On Planetesimal Formation: The Role of Collective Particle Behavior, in *Origin of the Earth and Moon* eds. Canup, R. M. and Righter, K. et al. (Tucson, AZ: Univ. Arizona Press), 2000, P.75
- Youdin, A. N., 2011, ApJ, 731, 99